Enhanced weathering in China's acidic rice fields offers potential agronomic co-benefits

Li Tan[1,*], E. Isadora Falkson[1], Tim Jesper Suhrhoff[2,1], Christopher T. Reinhard[3], Noah J. Planavsky[1,2,*]

[1]Department of Earth and Planetary Sciences, Yale University, New Haven, CT 06511, USA.
[2]Yale Center for Natural Carbon Capture, Yale University, New Haven, CT 06511, USA.
[3]School of Earth and Atmospheric Sciences, Georgia Institute of Technology, Atlanta, GA 30332, USA.

Corresponding author: noah.planavsky@yale.edu; li.tan@yale.edu

Abstract

China faces the converging challenges of farmland soil acidification, securing food security, and meeting carbon neutrality goals. Enhanced weathering (EW) offers a promising scalable carbon dioxide removal (CDR) pathway that can also deliver valuable agronomic benefits, but its potential for soil pH management, crop yield increases, and CDR in Chinese croplands is poorly constrained. Here, we develop a modeling framework to simulate co-benefits of basalt-based EW in acidic rice fields in China and conduct a spatially explicit national assessment. Focusing on the expected benefits from soil deacidification based on previous empirical data, EW can enhance relative rice yield by 4.61 ± 2.45% to 6.34 ± 3.98% by increasing mean soil pH by 0.68–1.02 units, resulting in a preliminary economic gain of USD 3.56 billion annually. This process also has the potential to simultaneously sequester 204.39 Mt CO_2 over 35 years based on strategic applications of an additional 50 t basalt ha^{-1} every ten years for fields where soil pH remains below 6.5. We find that the yield benefits alone would provide a gross agricultural revenue of USD 609 per tonne of gross CO_2 sequestered. Jiangxi, Hunan, Guangxi, and Guangdong persistently show the greatest co-benefits and should be prioritized as areas of early deployment. Our findings identify targeted EW deployment in China's acidic rice fields as a promising strategy to improve soil quality and support rice production, while potentially contributing to national CDR targets.

Introduction

The Paris Agreement has set the ambitious goal of limiting global warming to 1.5°C, which is crucial for avoiding the severe risks posed by climate change. It also operationalizes greenhouse gas mitigation through Nationally Determined Contributions (NDCs) aimed at limiting future warming[1]. Global warming temporarily exceeding the 1.5°C threshold is now effectively inevitable. Even in the most optimistic scenario, the warming will still reach at least 1.8°C before starting to decline[2]. To date, most of the ten largest fossil carbon emitting countries have failed to align with their 2030 NDC commitments, and even full implementation of these commitments would still imply median global warming of 2.6–3.1 °C[3]. In particular, some of the largest emitters, including China, India, and the United States, are not yet reducing emissions in line with their mitigation potential and need

to drastically ramp up their ambitions and actions[3,4].

Nevertheless, achieving climate targets through emission reductions alone is unlikely, and there is broad consensus that active deployment of carbon dioxide removal (CDR) strategies will be required to meet mitigation goals[5,6]. Enhanced weathering (EW)—the application of finely ground cation-rich rocks (e.g., basalt, wollastonite, etc.) to accelerate natural weathering reactions that consume atmospheric CO_2 and transfer it to the ocean for storage on climate-relevant timescales[7]—has emerged as a particularly promising CDR pathway, with initial estimates suggesting that deployment in major agricultural countries could remove 0.5–2 Gt CO_2 annually by 2050. Among these countries, China has the highest estimated EW potential[8,9] at 0.13–0.53 Gt CO_2 yr^{-1}.

As the world's largest emitter of both total CO_2 and agricultural carbon emissions, China has pledged to peak carbon emissions by 2030 and achieve carbon neutrality by 2060. These commitments, however, face major challenges[10]. Wang et al. estimated the annual average net CDR potential of 0.18–0.35 Gt CO_2 yr^{-1} under continuous multi-year basalt application across China's croplands[11], making a meaningful contribution to agricultural carbon neutrality. Meanwhile, China faces persistent pressure on food security, as it must feed 22% of the global population with only 9% of the world's arable land[12]. Further, excessive nitrogen fertilizer use has caused substantial acidification of Chinese farmland, posing a serious threat to crop production[12]. China is also one of the world's largest rice producers, with rice accounting for approximately 43% of national grain output. About 65% of the population depends on rice as a staple food, making it the cornerstone of national food security[13].

EW may be uniquely positioned to address both agricultural soil greenhouse gas (GHG) emissions and food security. Beyond its climate impact, EW has attracted increasing attention because of its multiple potential co-benefits, among which the greatest agronomic value is the neutralization of acidic soils[14,15]. Approximately 50% of the world's arable land is acidic and this proportion is increasing[16], which is a major agricultural constraint. Silicate rock flours have been used as fertilizers for decades[17], and numerous field trials have shown that EW can effectively regulate soil pH and boost yields in acidic soils[18], including for major crops such as rice, maize (corn), wheat, and soybean[14]. In regions where fertilizers are unavailable or prohibitively expensive, and in organic farming systems, powdered silicate rocks have been considered alternatives to conventional fertilization[19]. Basalt is an obvious candidate for agricultural EW in China, given concern in China about P and K limitation[20,21] (both of which basalt can supply[22,23]), its low heavy metal content, and high availability in multiple regions in China[24]. Furthermore, from a climate-mitigation perspective, using silicate rocks to alleviate soil acidity may be preferable to carbonate liming because it can improve yields without risking release of carbonate-derived CO_2[25]. Here, we develop a new estimate of the coupled CDR and agronomic benefits of periodic basalt application in Chinese rice systems.

Soil pH has been identified as a major driver of both rice yield and changes in soil organic carbon[26]. This is because pH affects almost every process in the soil system[27]. For paddy rice, near neutral soil conditions are generally most favorable for yield, typically 6.5–7.0 under flooding. Specifically, acidic soils depress rice yield by increasing soluble Al^{3+} and Mn^{2+} toxicity and exacerbating nutrient imbalances[28,29,30], with the result that changes in pH often have a bigger impact on yields than changes to nutrient pools alone. For instance, it has been found in some rice systems that while adding Ca alone did not improve yield or N uptake yield did increase with increasing pH, indicating that pH rather than Ca availability was the primary driver of the yield response[29]. In

another long-term experiment tracking yield responses to liming, crop yields improved as soil pH rose, even though Olsen-extractable P and exchangeable K did not show sustained increases[31]. These findings suggest that the yield benefits of EW are typically mediated through the alleviation of acidity constraints. Optimizing soil pH management can thus not only reduce agricultural GHG emissions, but also enhance crop yields and soil health[32].

Acidic to weakly acidic soil accounts for 77.75% of the rice growing area in China (Supplementary Fig. 1, Supplementary Fig. 2). Given this widespread prevalence of acidic soils as well as the need for CDR, deploying EW to raise soil pH, improve rice yield, and remove CO_2 appears both timely and well justified. Although several studies have modeled EW on cropland at the national scale[23], research in this area remains at an early stage, including in China[11]. Specifically, the weathering rate and CDR fluxes of EW when optimized for crop yields remain unclear, as does the quantitative response of crop yield to pH change.

We use an empirically grounded method to provide an estimate of the potential co-benefits of large-scale EW deployment in China's acidic rice fields. Specifically, we construct a spatially explicit modeling framework to evaluate soil pH elevation (ΔpH) and CDR capacity, and develop a quantitative system for rice yield that builds from a meta-analysis treating pH as a key explanatory variable. We simulate an initial basalt application of 50 t ha^{-1} to the upper 0–12 cm of acidic rice fields in 2026, with additional applications at the same rate in 2036, 2046, and 2056 only where modeled pre-application soil pH < 6.5. We quantify basalt dissolution, ΔpH, and gross CDR by tracking individual application cohorts, and estimate rice yield improvement (Δyield) using pH responses derived from a random-effects meta-analysis. We further integrate ΔpH, Δyield, and gross CDR into a comprehensive index of co-benefits (CIC) to identify priority deployment regions and assess robustness through sensitivity analyses of weathering kinetics, soil buffering, alkalinity export, feedstock CO_2 capacity, and index weighting. By integrating agronomic and climate benefits at the national scale, this study identifies where EW could most effectively support food security, sustainable soil management, and climate mitigation in China. We also provide a preliminary economic assessment—comparing expected gains from yield increases to tonnes of carbon removed (Fig. 1). While this is only a first assessment, it further bolsters the case that enhanced weathering could be an effective component of a mitigation package in China and that large-scale field trials are needed.

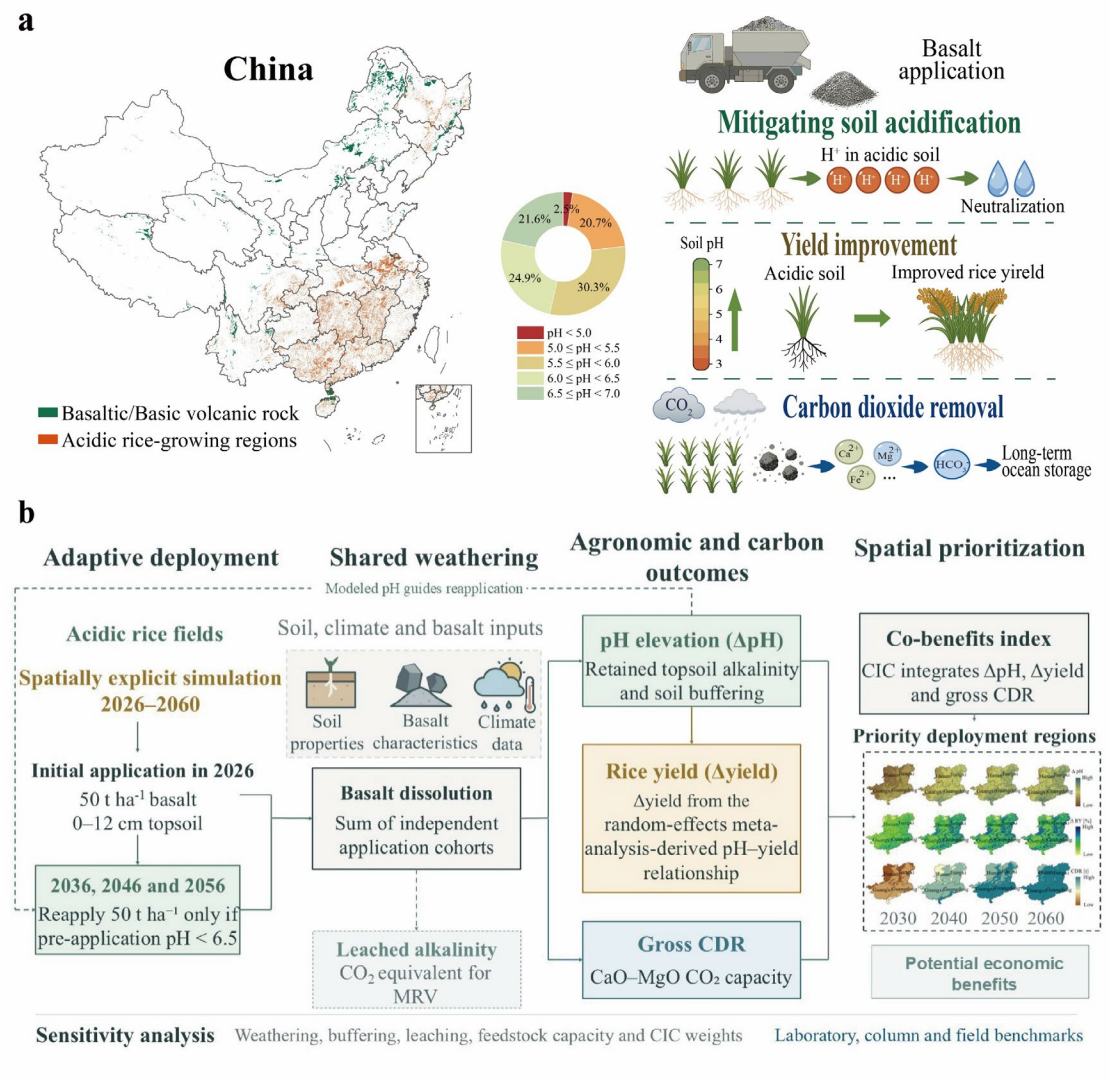


Fig. 1 | Mechanism and modeling framework for assessing EW co-benefits in China's acidic rice fields. a Spatial distribution of acidic rice-growing regions and basaltic/basic volcanic rocks in China, together with the initial soil pH composition of the assessed rice fields (percentages indicate proportion of soil area within each pH class in acidic rice-growing soils). The mechanism diagram summarizes the main EW outcomes considered in this study, including basalt application, mitigation of soil acidification, rice yield improvement, and gross CDR through basalt dissolution and alkalinity generation. **b** Overview of the spatially explicit modeling framework, including adaptive deployment strategy, data inputs, basalt dissolution modeling, assessments of ΔpH, Δyield (estimated from pH responses derived from a random-effects meta-analysis of rice yield), gross CDR, and CIC, provincial prioritization, preliminary economic assessment, and sensitivity analysis.

Results

Soil pH changes caused by EW

We simulated ΔpH across China's acidic rice fields using a spatially explicit basalt weathering model (see Methods). The baseline case was based on the measured basalt properties and selected weathering parameters, while alternative assumptions for soil buffering capacity (β_i), reactive surface area, basalt grain-surface dissolution rate (WR_{grain}), passivation parameter (α), and annual topsoil alkalinity leaching fraction (f_{leach}) were evaluated through sensitivity analyses. The spatial

distribution of ΔpH shows pronounced regional contrasts, with larger responses concentrated in southern, central, and southeastern China and smaller responses in northeastern China and parts of the southwest (Fig. 2a). Higher pH increments become more prominent across southern rice-growing regions between 2030 and 2040. These regional contrasts persist through 2050 and 2060, although the overall mean response declines slightly.

On average, ΔpH increases from 0.68 in 2030 to 1.02 in 2040, before decreasing to 0.96 and 0.90 in 2050 and 2060, respectively (Fig. 2b). A corresponding upward shift in the dominant density peak of mean ΔpH occurs between 2030 and 2040, followed by a shift towards lower increments in 2050 and 2060. After 2040, the density peak gradually shifts downward and remains below the mean. A secondary peak occurs at higher ΔpH, while a small concentration remains near the lower boundary. The widening box range and upper tails through time indicate greater heterogeneity among discrete locations as deployment proceeds. Meanwhile, the increasing separation between the mean and median suggests a more asymmetric distribution, with a subset of sites maintaining relatively large pH gains despite the declining dominant response (Fig. 2b). Accordingly, mean soil pH rises from an initial value of 5.96 to 6.64 in 2030 and 6.98 in 2040, before falling slightly to 6.86 by 2060 (Fig. 2c). The deterministic sensitivity envelope remains broad around the baseline trajectory (Fig. 2d).

The modest decline in ΔpH after 2040 is consistent with decelerating alkalinity release from aging basalt cohorts and continued alkalinity export from the topsoil. Because reapplication is restricted to sites with pH below 6.5 at the time of potential reapplication, fresh basalt inputs vary among sites. Where alkalinity losses exceed replenishment, retained topsoil alkalinity and the associated ΔpH decrease. The sensitivity trajectories based on variations in input parameters (see Supplementary Information) further indicate that the direction of ΔpH remains consistent across all tested parameter settings, although the magnitude varies among cases (Supplementary Fig. 3). ΔpH is most sensitive to β_i, WR_{grain}, and f_{leach}, with lower β_i and lower f_{leach} substantially increasing ΔpH, while lower WR_{grain} and higher f_{leach} markedly reducing it (Supplementary Fig. 8).

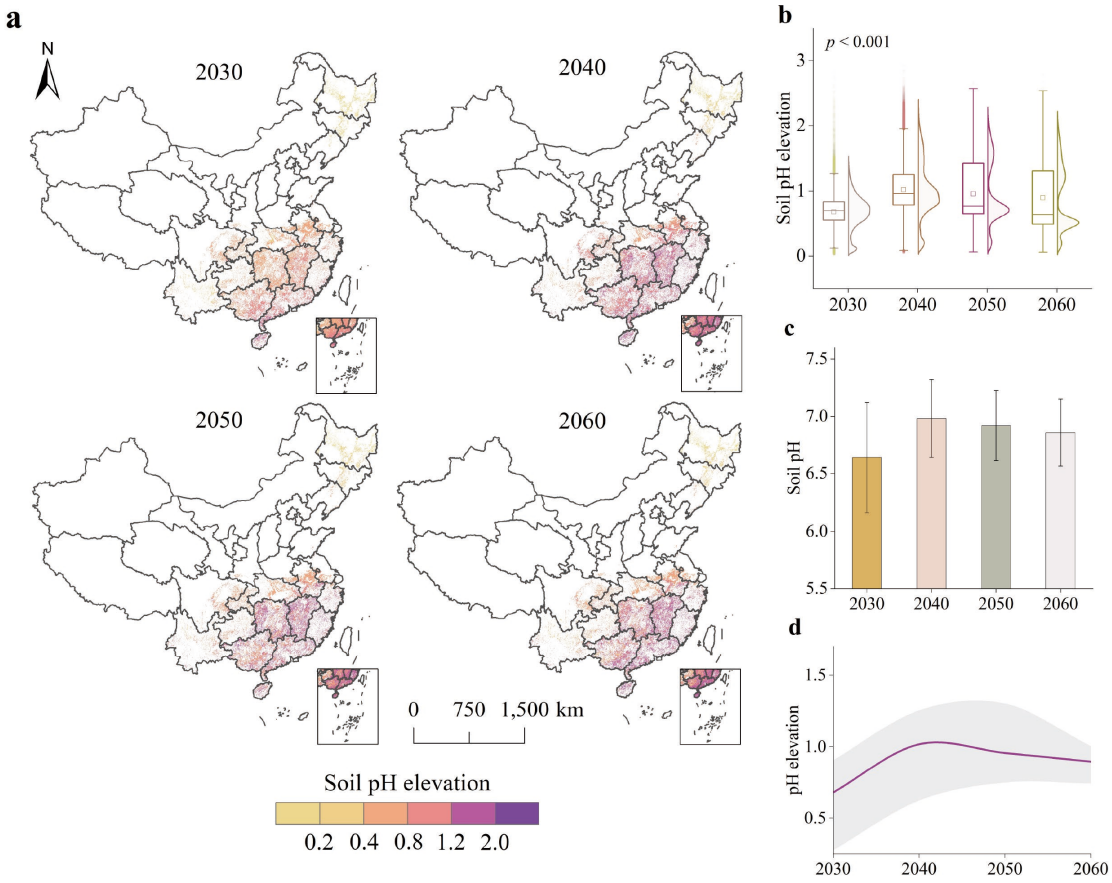


Fig. 2 | Soil pH changes in China's acidic rice fields following EW application from 2030 to 2060. a Spatiotemporal distribution of soil pH increment. Sampling sites represent acidic soils in rice-growing areas and grid cells are 1×1 km^2. Taiwan is not included in our assessment. **b** Distribution of ΔpH across grid cells at each time horizon. The left box indicates the interquartile range (25th–75th percentiles). The horizontal line within each box denotes the median, while the small box symbol reflects the mean. The error bars extend to the maximum and minimum values within 1.5 times the interquartile range. The half-violin curve on the right symbolizes the kernel density of the data distribution. The difference for each group comparison is statistically significant ($p < 0.001$). **c** Mean soil pH levels after EW application. Error bars represent standard deviation (SD)**. d** Sensitivity trajectory of mean ΔpH. The shaded band represents the deterministic sensitivity envelope, calculated as the minimum to maximum range of mean ΔpH across the tested sensitivity cases at each time horizon.

Rice yield improvement

Using compiled data for the response of Chinese rice yield to soil pH management (see Supplementary Methods and Supplementary Data 1), we fit within-study linear relationships between extracted pH values and relative yield (RY, normalized to the highest value within each study), as shown in Fig. 3b. Most observations fall within a pH range of approximately 5.0–6.5, and RY is generally higher in the 6.0–7.0 interval, where it is centered around 0.8–1.0. By contrast, under strongly acidic conditions, RY is noticeably lower, demonstrating a stronger yield response to ΔpH at low pH. Although individual studies show varying degrees of heterogeneity, positive slopes predominate overall. We also extracted the control group (CK) data from each study and performed linear regression to reflect standard practice, as shown in Fig. 3c. This confirms that, in the absence of additional management interventions, higher pH (up until pH 6.60) is positively

associated with rice yield. To quantify the RY increment per pH unit, we synthesize study-specific slopes using the DerSimonian–Laird method and visualize the results in a forest plot (Supplementary Fig. 5; see Methods and Supplementary Methods). Our results show that, within the pH range of 4.5–7.0, RY increases by approximately 1.07% for every 0.1-unit increase in pH (95% confidence interval (CI): 0.66%–1.48%), and we determine the yield increments associated with different pH intervals following robustness checks and accounting for diminishing returns (Supplementary Fig. 5; see Supplementary Methods).

The relative yield improvement (ΔRY) response derived from simulated weathering-derived increases in soil pH is mainly concentrated in southern and central China, especially in the Middle and Lower Yangtze Valley Plain, the southern rice belt, and along the southeast coast. Yield gains become more widespread across the major rice fields starting in 2040, and the expansion tends to stabilize in 2050 and 2060 (Fig. 3a). Consistent with the pH trend, mean ΔRY rises from 4.61 ± 2.45% in 2030 to 6.34 ± 3.98% in 2040, slightly decreases to 6.22 ± 4.19% in 2050 and 6.02 ± 4.13% in 2060, but the maximum value increases, reaching 21.83% and 21.38% in 2050 and 2060, respectively (Fig. 3d). At the provincial level, the results reveal a clear north-south gradient (Fig. 3e). By 2030, eight regions exhibit positive anomalies relative to the overall mean ΔRY, particularly in Hong Kong, Hainan, Guangdong, Fujian, and Jiangxi. By 2040, the mean ΔRY in the provinces of south China and the middle and lower reaches of the Yangtze River is more pronounced, with strong interprovincial responses expanding northward and inland, and some areas nearly doubling (Fig. 3e). In contrast, yield gains in northern provinces remain generally lower. In 2050 and 2060, ΔRY in most regions experiences varying degrees of decline. Compared to 2040, fifteen provinces report a decline in 2050, and twenty provinces in 2060. We therefore infer that rice yield benefits are likely to peak around 2040, with diminishing returns thereafter.

The sensitivity trajectory in Fig. 3f also shows that the largest ΔRY occurs around 2040 and marginal growth declines thereafter. Compared with ΔpH, the sensitivity range of ΔRY is more constrained, suggesting that the capped pH to yield response moderates the propagation of parameter uncertainty into estimated yield benefits. The sensitivity analysis indicates that, under all tested parameter settings except for the lower WR_{grain} scenario, which will result in continuous mean ΔRY growth from 2030 to 2060, ΔRY is expected to decline to varying extents after 2040 or 2050, though the differences are generally small (Supplementary Fig. 6). Compared to the baseline case, the strongest parameter sensitivities are, in order, f_{leach}, WR_{grain}, and β_i, reflecting their control over ΔpH and the subsequent yield response (Supplementary Fig. 8).

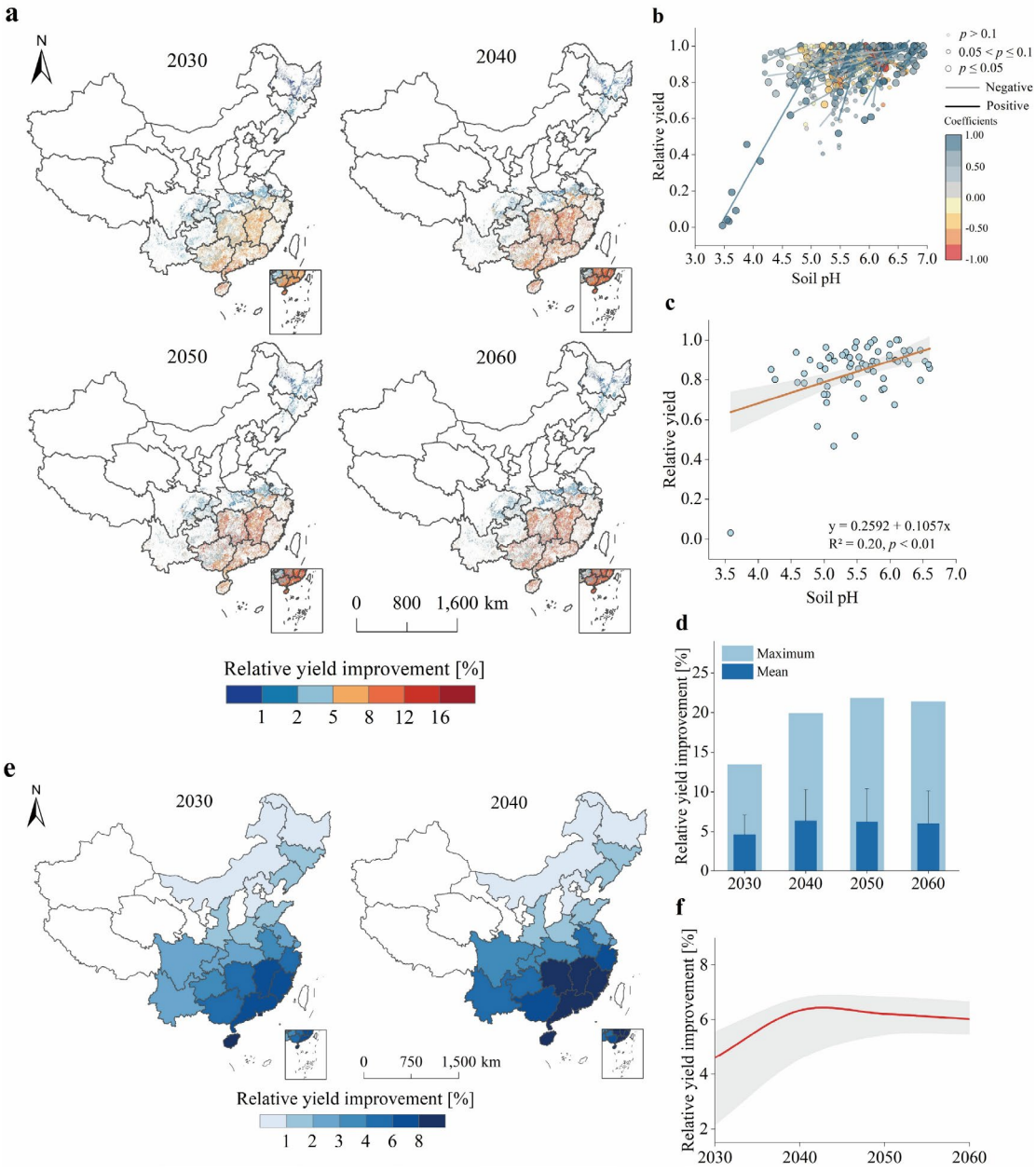


Fig. 3 | Rice relative yield improvement and its spatiotemporal distribution from 2030 to 2060. a Spatiotemporal distribution of ΔRY driven by soil pH change. **b** Study-specific linear fitting between soil pH and relative rice yield across 71 studies. Each point represents an extracted observation and each line reflects a within-study linear fit. Line and point color indicate the fitted coefficient, and symbol size indicates the significance level. **c** Linear regression for all extracted CK, supporting descriptive evidence for the positive tendency of pH and yield under standard practice. The slope is 0.1057 and the intercept is 0.2592. The error envelope reflects a 95% confidence interval. The Supplementary Methods report robustness check after excluding pH values below 4.5. **d** Statistical summary of ΔRY. Bars, arranged from wide to narrow, represent the maximum and mean values, with the minimum value being 0.05%. Error bars indicate SD. **e** The spatial aggregation of grid cell yield responses at the province level. The periods 2030 and 2040 show the fastest increases in RY. **f** Temporal sensitivity of mean ΔRY from 2030 to 2060. The shaded area indicates the deterministic sensitivity range derived from the minimum and maximum mean ΔRY among the tested sensitivity cases at each time horizon.

Carbon drawdown potential from EW

Gross CDR was estimated by summing contributions from basalt cohorts applied under the adaptive reapplication scheme, using the same modeled dissolved fractions as in the soil pH simulation and the CaO- and MgO-derived feedstock CO_2 capacity. CDR sensitivity analyses focused on effective reactive surface area, WR_{grain}, and α, with β_i and f_{leach} held at their reference values when determining reapplication eligibility. We also quantified the CO_2 equivalent of weathering-derived alkalinity leached from the modeled topsoil to provide a reference for measurement, reporting, and verification (MRV). Complete models are provided in the Supplementary Methods. EW generates a clear and increasing cumulative gross CDR signal from 2030 to 2060 (Fig. 4). Spatially, higher CDR capacity is mainly distributed across the southern and central rice-growing regions, broadly overlapping with areas of stronger EW alkalization. The modeled CDR footprint becomes more extensive, while the spatial pattern remains relatively stable and the cumulative magnitude continues to increase (Fig. 4a). The temporal trajectory of gross CDR shows a rapid early increase, followed by a slightly slower but steady accumulation phase. Under the baseline case, gross CDR rises from 65.13 Mt CO_2 in 2030 to 204.39 Mt CO_2 by 2060 (Fig. 4b). The cumulative CO_2 equivalent associated with leached alkalinity increases from 10.06 Mt CO_2 in 2030 to 48.34, 91.47, and 130.49 Mt CO_2 in 2040, 2050, and 2060, respectively, reflecting the progressive export of weathering-derived alkalinity from the topsoil (Fig. 4b).

The deterministic sensitivity envelope (Fig. 4b) indicates that gross CDR is primarily controlled by assumptions directly affecting basalt dissolution. Lower WR_{grain} and reduced effective reactive surface area produce the strongest decreases in cumulative CDR, whereas higher WR_{grain} and increased reactive surface area raise the estimates above the baseline case. Changes in α have a more moderate but persistent effect on long-term accumulation, with weaker rate deceleration increasing CDR and stronger deceleration reducing it (Supplementary Fig. 7 and Supplementary Fig. 8). Overall, these results suggest that uncertainty in basalt reactivity and field-effective surface area is the main source of variation in projected CDR, while the increasing temporal trend remains consistent across all tested cases. Hunan, Jiangxi, Guangxi, Guangdong, and Anhui contribute the largest amounts of gross CDR, while most northern and northwestern provinces contribute relatively little to gross CDR, indicating that the national CDR potential is concentrated in major southern and central rice-producing provinces (Fig. 4c). It is important to note that basalt can be milled to achieve faster dissolution rates and potentially overcome issues of passivation. The presented results cover what we consider to be a reasonable range of weathering outcomes, but they are meant to be illustrative to provide motivation for field trials. Additionally, we note that these results do not take into account downstream carbon leakage, which has been estimated to be at least a roughly ~10% inefficiency in EW CDR process[33].

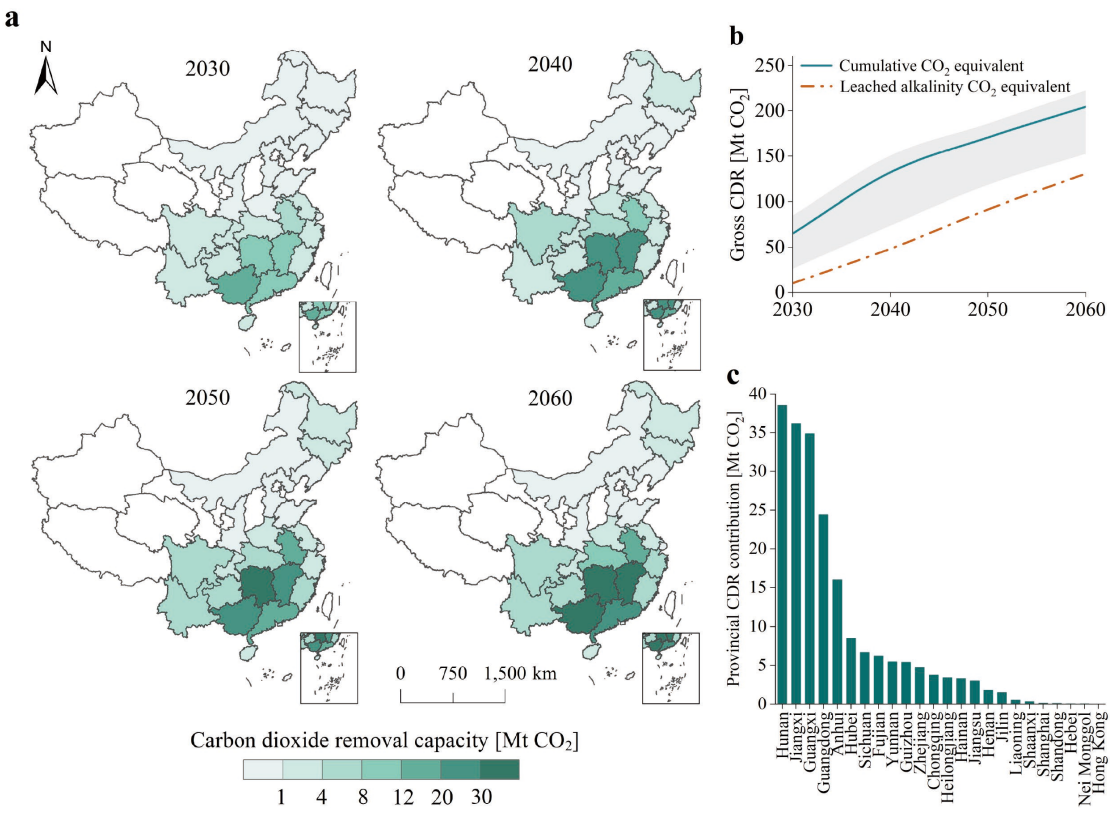


Fig. 4 | Carbon dioxide removal capacity via EW in China's acidic rice fields from 2030 to 2060. a Spatiotemporal distribution of carbon drawdown potential. **b** Cumulative gross CDR and CO_2 equivalent of weathering-derived alkalinity leached from the modeled topsoil from 2030 to 2060. The shaded area summarizes the spread of CDR estimates caused by alternative weathering parameter assumptions, calculated from the lowest and highest cumulative CDR values among the tested sensitivity cases at each time horizon. **c** Provincial contributions to gross cumulative CDR by 2060.

Comprehensive evaluation of potential co-benefits

To integrate the three modeled co-benefits, we calculated a comprehensive index of co-benefits (CIC) using provincial mean ΔpH, provincial mean ΔRY, and cumulative provincial gross CDR. We include ΔpH as a separate indicator because, beyond its effects on crop yield, alleviating soil acidity can also reduce heavy metal mobility and associated environmental and food safety risks (see Supplementary Methods). The main CIC uses equal weights for the three indicators, while we evaluate CIC sensitivity by assigning higher priority to ΔpH, ΔRY, or CDR individually. Detailed normalization procedures and weighting schemes are provided in the Supplementary Methods. The overall CIC values increase progressively from 2030 to 2060, exhibiting a stepwise growth (Fig. 5b). Under the equal weight setting, the strongest increase occurs between 2030 and 2040, suggesting that the main accumulation of comprehensive co-benefits occurs during the early to middle stage after basalt application. After 2040, CIC growth becomes slower, consistent with the gradual deceleration of weathering and the reduced marginal yield response as soil pH approached or exceeded the calibrated response range. Jiangxi, Hunan, Guangxi, and Guangdong perform strongly throughout the study period, and the CIC of most provinces peaks in 2040 (Fig. 5a). Guangxi has the largest CIC after five years of EW application, closely followed by Guangdong and Jiangxi, with a slight gap between them, while Hunan follows Hainan but already ranks among the

major priority provinces. From 2040 onward, Jiangxi has become the highest-ranking province and maintained its leading position through 2060. Hunan shows strong persistence and increases in rank, becoming the second highest province in 2040, 2050, and 2060. Guangxi and Guangdong remain consistently important, although their CIC values gradually declined in the later stage (Fig. 5c). This indicates that Jiangxi, Hunan, Guangxi, and Guangdong represent the core regions where EW deployment is most likely to generate strong combined benefits.

The warm and humid conditions of southern and central China may further support basalt dissolution, while the initially acidic rice field soils provide substantial potential for co-benefits related to alkalization and yield. The CIC weighting sensitivity analysis shows that the main temporal and spatial patterns are generally robust to alternative weighting assumptions. Although the internal ranking of provinces varies when greater weight is assigned to ΔpH, ΔRY, or CDR, Jiangxi, Hunan, Guangxi, and Guangdong remain among the most important priority regions in the later periods (Supplementary Fig. 9).

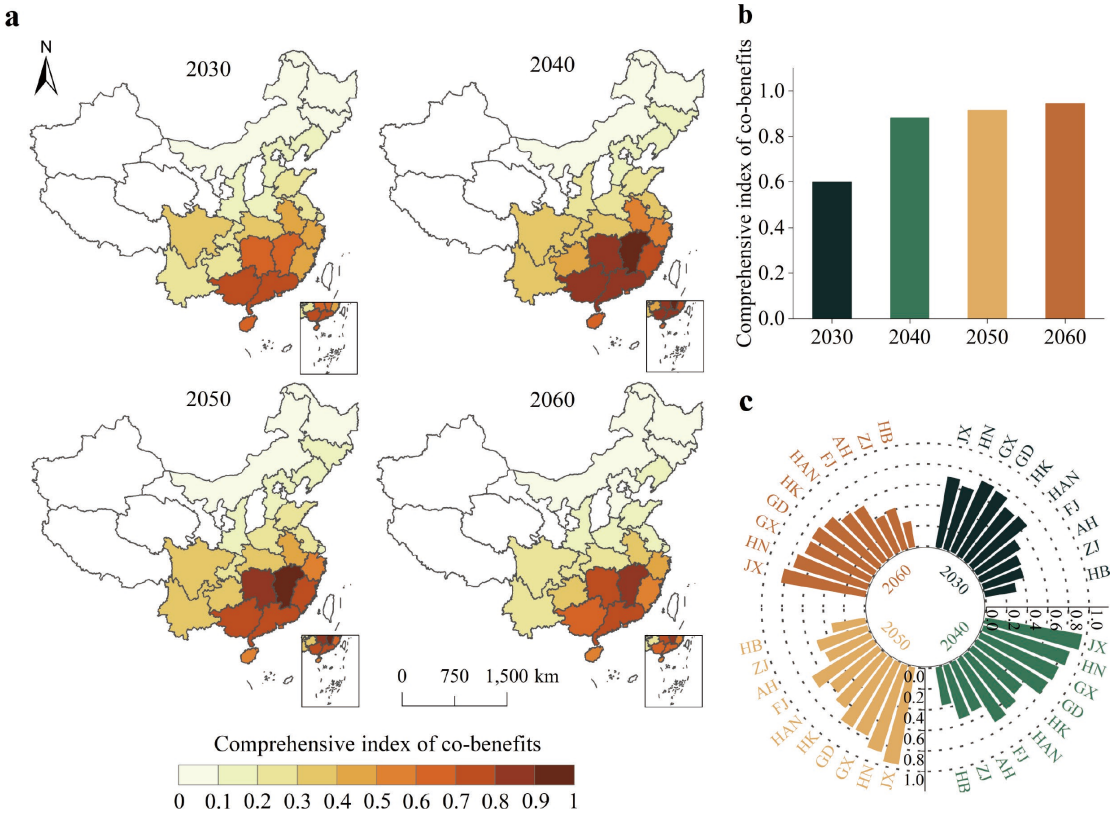


Fig. 5 | Trends and priority regions of comprehensive co-benefits in China's acidic rice fields. a Spatial patterns of CIC from 2030 to 2060. **b** Temporal trend of the overall equal weight CIC from 2030 to 2060. The bars show overall CIC values for each period, indicating the progressive accumulation of integrated co-benefits over time. **c** Top ten provinces ranked by equal weight CIC from 2030 to 2060. The axis scale of CIC ranges from 0 to 1. Province abbreviations: JX, Jiangxi; HN, Hunan; GX, Guangxi; GD, Guangdong; HK, Hong Kong; HAN, Hainan; FJ, Fujian; AH, Anhui; ZJ, Zhejiang; HB, Hubei.

Discussion

Soil acidification in Chinese cropland was most pronounced from the 1980s to the 2000s, during which the average pH of major farmlands declined by 0.5 units[34]. Although Zhang et al. reported that the acidification trend generally began to slow around 2013, this conclusion depends on the

assumed N fertilizer consumption scenarios and even with further reductions in chemical N fertilizer application, soil pH is unlikely to recover to levels observed in the 1980s[35]. Zhu et al. also predict that pH in China's rice fields will continue to decline. Under the business-as-usual fertilizer management scenario (annual N fertilizer increase of 1%), the average pH in rice fields decreases by 0.86 units from 2010 to 2050[12]. Even under the N2020 scenario (i.e., N input increases by 1% annually until 2020 and then stops increasing in accordance with the Ministry of Agriculture's policy), the pH decrease is still 0.76 units[12]. Further, data from two national soil surveys (1985–1990 and 2006–2010) in China indicate that in southern China, the average pH of paddy soils dropped from 5.81 to 5.19 over this period[36].

An increase in soil pH and associated agronomic impacts are the most obvious co-benefit generated through EW with basalt, limestone, and other silicate minerals. These arguments are supported by decades of laboratory, greenhouse, and field experiments focused on agronomic response[14]. Liming is widespread and there are numerous papers on the agronomic benefits, including in rice systems[16,37,38]. However, there are also well-documented examples of silicate providing sustained pH increases[14]. For example, Zacharias et al. monitored a ΔpH of 0.15–0.24 units after 13 months of basalt application, with soils of higher initial acidity showing a greater rise in pH[39]. In maize pot experiments, only 3.5 t ha^{-1} of olivine raised pH by 0.4–0.5 units[40]. Some experimental results have reported that pH changed by almost 2 units[41,42]. A recent data compilation furthermore demonstrates that agronomically sensible application rates are sufficient to elevate soil pH via silicate powder addition[14]. This response is closely related to the initial pH conditions, and appears to be most effective in neutralizing acidic soils[14]. Our results suggest that EW could reduce the proportion of acidic arable land (pH < 6.5) in China's rice-growing areas from an initial 61.09% to 3.83% by 2040, with an average elevation of 0.68 pH units over the first five years of deployment, which would greatly alleviate soil acidification in Chinese farmland. Although the magnitude of pH increase slightly decreases after 2050, it remains close to 1.00 unit, which is also consistent with the range reported in field trials of silicate-based EW.

Our findings are generally consistent with existing case studies and data synthesis efforts. A meta-analysis of 121 global field studies by Wang et al. pointed out that liming acidic soils can drive an average pH rise of 0.9 units, promoting rice yield by 11.9%[16]. This corresponds to a 1.32% increase in rice yield per 0.1 increment in soil pH, broadly consistent with our estimate of 1.07% (ranging from 0.54% to 1.23% across each pH interval of 4.5–7.0, see Supplementary Methods). Another study of compiled paired crop yield and soil pH observations for wheat, maize, and rice across 50 studies in China found that under most scenarios acidification leads to substantial RY losses, with rice showing the largest decline among the three crops. Under a scenario of constant current N input, soil acidification was projected to reduce rice yields by 20% by 2030 and by nearly 30% by 2050[12]. Field-scale and experimental studies further support our findings, showing that basalt-based EW can produce substantial yield gains in rice systems. A study in Liaoning found that applying 5 t ha^{-1} of wollastonite for five months boosted rice yield by 12%[43]. Another rice paddy mesocosm experiment showed a 20.7% yield increase at 36 t ha^{-1} basalt. These gains were accompanied by 11.3 t CO_2 ha^{-1} sequestration and increased silicon concentrations[44]. Using our framework and the conditions of these studies we would predict that boosting pH by 1.02 units results in a mean ΔRY of 6.34 ± 3.98 (SD) % over the first 15 years, suggesting our approach may be conservative.

Although basalt-based EW operates through mechanisms broadly analogous to liming via soil

pH modification, basalt may offer enhanced agronomic benefits beyond those achieved by liming. On the other hand, the positive impact of increasing soil pH may also have a limit. Alkaline soils, especially > 7.5, could lower yields by reducing the availability of micronutrients and promoting P precipitation as Ca phosphates[45,46,47]. Beerling et al. also pointed out that a pH > 7.5 may pose a risk of excessive alkalinity and emphasized the need for continuous monitoring of soil pH, which is a standard farm management practice[23]. However, the areal extent of rice lands with pH > 7.5 is generally very low in our reference model, amounting to 2.32% in 2030, 8.05% in 2040, 3.90% in 2050, and 1.10% in 2060.

Based on analysis of actual rice production over the past decade, we find that China's total population grew but rice production declined from 2015 to 2024, and the current production is lower than that of 10 years ago (Supplementary Fig. 10). When viewed in light of the potential impact of soil acidification, this raises concerns about whether rice yield capacity can fully meet future grain demand. Among the provinces for which mean ΔRY exceeds 8% by 2040, Hunan, Jiangxi, and Guangdong rank first (2,675.1 × 10^4 t), third (2,065.5 × 10^4 t), and eighth (1,123.6 × 10^4 t), respectively, in actual 2024 rice production (Supplementary Fig. 11). These findings indicate that provinces with the largest simulated yield gains largely coincide with major rice-producing regions in China and that central and southern China retain substantial potential for yield enhancement through EW. The actual production in the priority deployment regions we suggest (Jiangxi, Hunan, Guangxi, and Guangdong) accounts for 33% of the total production (Supplementary Fig. 11). Targeted EW deployment could therefore contribute to China's food security by improving agricultural productivity in some of its most important rice-producing regions.

Agricultural emissions have become the second largest source of greenhouse gases in China after the energy sector. In this context, agricultural EW deployment could play a key role in accelerating progress toward China's carbon neutrality commitments. In our baseline case, EW deployment in China's acidic rice fields produces 204.39 Mt CO_2 of gross cumulative CDR by 2060. Cong et al. used a life cycle assessment (LCA) framework and a shrinking-core model to evaluate basalt-based EW across China, reporting that nationwide basalt application with a particle size below which 80% of particles pass screening ($p80$) of 100 μm could sequester 76.55 Mt CO_2 by 2060, while a scenario with $p80$ = 10 μm could sequester 469.15 Mt CO_2 by 2060[48]. Our estimate is over 2.5 times higher than their reported value for $p80$ = 100 μm, and roughly 40% of their $p80$ = 10 μm scenario. After accounting for the fact that LCA-based deductions are often on the order of 5%–25% of gross removal[4,49], our estimated CDR potential remains substantial.

The contribution of rice-field EW should also be considered in the context of China's broader EW potential and future CDR requirements. Wang et al. recently estimated that a single basalt application across Chinese croplands could achieve 0.44–0.79 Gt CO_2 of cumulative net removal by 2100, while repeated applications could meet 5–30% of China's annual negative emissions requirements by 2060[11]. These inferred annual rates are larger than the values derived here, but they also cover a much larger agricultural area (rice-growing areas account for approximately 24% of China's total cropland[50]) and different deployment scenarios and time periods than our assessment. Importantly, whereas they focused on CDR potential and costs, our study specifically targets acidic rice fields, links adaptive basalt reapplication to soil pH improvement, and quantifies the associated rice yield benefits. Deng et al. reported that achieving carbon neutrality in China may require annual deployment of negative emissions technologies (NETs) ranging from 0.01 to 2.91 billion tonnes CO_2 between 2050 and 2060[51]. In our simulation period, 0.006 billion tonnes CO_2 can be

removed annually, reaching 0.013 billion tonnes CO_2 yr^{-1} in the first five years of deployment, which falls within the lower limit range reported by them. While this represents a relatively modest contribution to China's projected NET requirements, our assessment considers only acidic rice fields rather than all agricultural land. Rice-field EW could therefore complement other CDR approaches, while simultaneously improving soil pH and crop yields, particularly in warm, humid, and acidic regions.

The feedstock capacity sensitivity further shows that basalt chemistry strongly affects the estimated CDR potential. Our baseline case used measured basalt compositions of 5.3% CaO and 2.4% MgO. However, national basalt data indicate that Chinese basalts contain, on average, 9.10% CaO and 7.35% MgO[52]. When the CaO and MgO contents were replaced with the higher Chinese average values, gross cumulative CDR increased to approximately 457.83 Mt CO_2 by 2060, about 2.24 times higher than the reference estimate (Supplementary Table 3 and Supplementary Methods). This indicates that the CDR contribution of rice field EW may be substantially higher where suitable Ca- and Mg-rich basalt feedstocks are available, emphasizing the importance of regional feedstock selection in future deployment assessments.

China’s abundant basalt resources also provide a strong basis for large-scale EW deployment. Major basalt reserves, which are commonly used in road construction, occur in southwestern and northeastern China, as well as in the Leizhou Peninsula of southern Guangdong and northern Hainan, with additional deposits scattered across eastern provinces. As a result, many provinces can source basalt locally for transport and application[48]. Under our adaptive decadal reapplication strategy, the total cumulative basalt demand from 2026 to 2056 is estimated at 1.90 Gt. The initial application requires 1.23 Gt, equivalent to approximately 8.1% of China's annual aggregate production of 15.2 Gt in 2024[53]. Over the subsequent 30 years, only an additional 0.67 Gt of basalt is required. The substantial scale of China's existing aggregate industry, particularly its extensive crushed-stone production[54], further supports the potential for large-scale EW deployment. Jiangxi, Hunan, Guangxi, and Guangdong—the provinces with the highest CIC values—are geographically adjacent and near major southern basalt deposits (Fig. 1a), lowering costs and lifecycle emissions associated with feedstock transport. These regions could therefore be prioritized for EW-based agricultural land management. Together with the long-standing use of crushed limestone to reverse soil acidification and manage fertilizer regimes in cropland[3], globally mature mining and grinding technologies, and the high level of agricultural mechanization in southeastern China, this illustrates that large-scale, rapid deployment may be feasible within the next few decades. Nonetheless, public trust, farmer acceptance, and economic viability need to be carefully considered before implementation[8].

Beyond soil improvement and carbon removal, EW may also provide substantial economic benefits through increased rice production. Based on an estimated mean yield improvement of 5.46% over 2026–2060, a preliminary economic assessment suggests that EW could generate approximately USD 3.56 billion in annualized gross rice revenue benefits across China's acidic rice fields, corresponding to USD 124.54 billion over 35 years. Relative to the modeled cumulative gross CDR of 204.39 Mt CO_2, this represents an additional agricultural revenue benefit of approximately USD 609 per tonne of CO_2 removed (see Supplementary Methods for calculation). These estimates assume that modeled relative yield improvements translate proportionally into rice production gains, with constant baseline productivity and rice prices, and exclude the cost of EW deployment. However, they provide a basis for evaluating the breakeven cost of deployment that can be defrayed

by increased yield and highlight the importance of integrating agronomic benefits into technoeconomic assessments of EW deployment. Nonetheless, it is worth noting that this gross agricultural revenue benefit per tonne of modeled CDR is well beyond typical estimates of basalt deployment costs[55].

The magnitude of these benefits will depend, in part, on how soil acidification and basalt dissolution evolve under future conditions. Nitrogen fertilizer has been a dominant driver of cropland acidification in China, although future policy and management changes could partly slow or reverse this trend[12,34]. Soil pH trajectories are uncertain and likely nonlinear because they reflect interactions among ongoing acid inputs, soil buffering, and pH-dependent mineral dissolution[56,57]. Future modeling should couple EW kinetics with dynamic acidification scenarios linked to fertilizer management and atmospheric pollution. Basalt dissolution rates depend on solution pH, but experimental studies across acidic to alkaline conditions show that the response is mineral- and element-specific and is not monotonic across the full pH range[58]. Therefore, we did not impose a single empirical pH feedback multiplier on the national-scale simulations. Furthermore, although the model accounts for topsoil alkalinity retention and leaching, the subsequent fate of exported alkalinity remains unresolved and its CO_2 equivalent should not be interpreted as realized or net CDR[59]. Future coupling with mechanistic soil reactive transport models and regional life-cycle assessments could better constrain alkalinity transport, carbon retention, and net removal[60].

Our findings highlight the importance of considering agronomic requirements when assessing the CDR potential of agricultural EW. Unlike scenarios assuming repeated rock applications primarily to maximize CDR[3], our approach restricts further basalt applications based on soil pH. While such constraints may limit the total CDR potential compared with unconstrained deployment scenarios, they provide a more realistic basis for assessing EW in agricultural systems. Importantly, the potential improvements in soil quality and crop yields may provide a strong incentive for EW deployment in their own right, with carbon removal as an additional benefit.

Methods

Soil pH neutralization

We assumed basaltic rock with a *p*80 of 35 μm and an initial application of 50 t ha^{-1} in 2026, with additional 50 t ha^{-1} applications in 2036, 2046, and 2056 only when modeled soil pH immediately before reapplication was < 6.5, to simulate EW deployments. We combined these parameters with rice soil attributes to estimate the potential alkalinity supplied by basalt weathering at each soil site. The basalt characteristics and basis are described in Supplementary Methods and Supplementary Table 1. Following a general EW framework, crushed basalt applied to the topsoil was considered as the source of alkalinity released through weathering, and the neutralizing effect was attributed to the Ca- and Mg-bearing oxide fraction of the basalt (see Supplementary Methods for the weathering reaction equation). We then utilized a surface area normalized (based on specific surface area; SSA) dissolution rate formula accounting for the impact of temperature and precipitation to represent the spatial differences in effective weathering intensity, as the silicate weathering rates are strongly governed by mineral surface area, reaction kinetics, and hydrological conditions[61,62]. Long-term field weathering rates typically decline relative to initial or laboratory rates due to time-dependent surface evolution, transport limitations, and surface passivation, which is consistent with field scale silicate weathering behavior[63]. Hence, to avoid unrealistically long-term constant dissolution, we adopted a decelerating (DL) dissolution scheme to determine the cumulative dissolution fraction of

basalt. Additionally, we estimated soil buffering capacity from soil organic matter and clay content using the Murphy and Helyar relationship[64,65]. To represent removal of weathering-derived alkalinity from the modeled topsoil, a first-order annual leaching fraction was applied to the cumulative alkalinity stock. Weathering-derived alkalinity retained in the 0–12 cm layer was updated annually after applying an annual leaching fraction, and the retained alkalinity was used to estimate ΔpH[66]. Detailed methods and sensitivity analysis are provided in Supplementary Methods.

Rice yield increases

We conducted a random-effects meta-analysis to quantify the rice yield response to pH change in acidic soils from available literature, and the collection process and eligibility criteria are described in greater detail in Supplementary Methods. From the 71 eligible studies, paired observations of soil pH and rice yield were extracted, and yield was normalized relative to the highest reported yield within each study (RY) to enable comparison on a common scale. To minimize bias from differences in climate, soil type, cultivar, and background management, we first estimated two relationships between RY and pH using within-study linear regression and an overall linear regression using the CK observations. We then synthesized the study-specific slopes using a random-effects meta-analysis. A random-effects model was used because it explicitly accounts for heterogeneity among studies[67]. Additionally, we focus on pH changes within the range 4.5–7.0. The final pooled response coefficient was therefore estimated using only observations in this range, thereby improving consistency between the calibration range and its intended application. Yield benefits were capped at pH 7.0, which means that pH increases up to 7.0 were credited as positive yield benefits, but no additional positive yield benefit was assigned beyond pH 7.0. The Hartung–Knapp refinement was employed to provide more robust uncertainty estimates for the pooled effect, which is advantageous when heterogeneity is substantial or when study-specific precision differs markedly[68,69]. We also adopted a bounded fractional response model to assess whether the relationship between pH and yield exhibited diminishing returns at higher pH values, meaning that as reactive minerals are progressively consumed and soil tends to become less acidic, the marginal returns diminish over time, which is better suited to fractional outcomes than ordinary linear models. The pooled slope was used to quantify the overall response, whereas the marginal effects for specific pH bins were used to calculate yield gains from projected pH changes. This workflow follows the logic of dose–response meta-analysis, which is specifically designed to synthesize quantitative exposure–response relationships across independent studies[70,71]. The forest plot and modeling steps are provided in Supplementary Methods and Supplementary Fig. 5.

Carbon dioxide removal

To estimate gross CDR from basalt-based EW, we adopted a spatially explicit grid cell framework[3,19]. First, following standard EW accounting practices, we estimated the ideal gross maximum stoichiometric CDR capacity of the basalt feedstock from its CaO and MgO contents and the application rate, because these divalent oxides provide the principal acid neutralizing and CO_2 consuming capacity of silicate weathering[72]. Second, to maintain internal consistency between soil alkalization and CDR calculations, we used the same cumulative decelerating dissolved fraction for each applied basalt cohort for both ΔpH and gross CDR estimation. Thus, the released Ca and Mg alkalinity used for soil pH neutralization and modeled gross CDR were derived from the same modeled basalt weathering trajectory. The adaptive pH-based application schedule was also shared

by the pH and CDR calculations. This decelerating formulation represents progressive field-scale rate decline associated with surface evolution, secondary coatings, transport limitation, and passivation[73]. Finally, we converted cell level CDR estimates to gross CDR totals by combining basalt application intensity with grid cell area and summing across the study domain. As a secondary MRV metric, we calculated the CO_2 equivalent of weathering-derived alkalinity leached from the modeled topsoil[74,75]. We also conducted alternative assumptions as the sensitivity analysis, and detailed methods are provided in Supplementary Methods.

Data availability

The distribution data of rice-growing areas in China were obtained from Chinese Academy of Sciences Discipline Data Center for Ecosystem/National Ecosystem Science Data Center (https://www.nesdc.org.cn and https://doi.org/10.1088/1748-9326/ab80f0). Soil properties data were sourced from National Tibetan Plateau/Third Pole Environment Data Center (https://data.tpdc.ac.cn and https://doi.org/10.5194/essd-17-517-2025). Climate data were derived from Resources and Environmental Science and Data Center (www.resdc.cn). Rice yield and population data in China were sourced from China Statistical Yearbook, National Bureau of Statistics of China (https://www.stats.gov.cn). The distribution data of basaltic/basic volcanic rock were obtained from the Global Lithological Map database (GLiM) (https://doi.org/10.1594/PANGAEA.788537). China's national average rice yield was sourced from National Bureau of Statistics of China (https://www.stats.gov.cn). The rice procurement price was sourced from Shanghai National Grain Trading Center (https://www.shyouandme.com).

Code availability

The source codes used to calculate soil pH changes and gross carbon dioxide removal are publicly available on Zenodo at: https://doi.org/10.5281/zenodo.23987571.

Funding statement

TJS acknowledges funding from the Yale Center for Natural Carbon Capture. NJP acknowledges funding from Environmental Defense Fund and the Fund for Science and Technology.

Competing interests

CTR and NJP serve as scientific advisors to CREW Carbon, a company that generates alkalinity in wastewater treatment plants using lime addition but does not work on terrestrial Enhanced Weathering in agricultural fields. NJP and CTR were co-founders of the Enhanced Weathering supplier Lithos Carbon but have no financial ties to the company. All other authors declare no competing interests.

Additional information

Supplementary information

Description of Additional Supplementary Files

Supplementary Data 1

Supplementary Data 2

Supplementary Data 3

References

1. United Nations Framework Convention on Climate Change (UNFCCC). *Paris Agreement* (2015).

2. United Nations Environment Programme. Limiting Overshoot: Navigating exceedance of 1.5°C and pathways towards return. *Nairobi* (2026).

3. Beerling, D.J. et al. Potential for large-scale CO_2 removal via enhanced rock weathering with croplands. *Nature* **583**, 242–248 (2020).

4. Eufrasio, R.M. et al. Environmental and health impacts of atmospheric CO_2 removal by enhanced rock weathering depend on nations' energy mix. *Commun. Earth Environ.* **3**, 106 (2022).

5. Amann, T. et al. Enhanced Weathering and related element fluxes–a cropland mesocosm approach. *Biogeosciences* **17**, 103–119 (2020).

6. Intergovernmental Panel on Climate Change. Climate change 2022: impacts, adaptation and vulnerability. Contribution of Working Group II to the sixth assessment report of the Intergovernmental Panel on Climate Change. *Cambridge University Press* (2022).

7. Goll, D.S. et al. Potential CO_2 removal from enhanced weathering by ecosystem responses to powdered rock. *Nat. Geosci.* **14**, 545–549 (2021).

8. Beerling, D.J. et al. Challenges and opportunities in scaling enhanced weathering for carbon dioxide removal. *Nat. Rev. Earth Environ.* **6**, 672–686 (2025).

9. Baek, S.H. et al. Impact of climate on the global capacity for enhanced rock weathering on croplands. *Earths Future* **11**, e2023EF003698 (2023).

10. Guo, F.X. et al. Improving food security and farmland carbon sequestration in China through enhanced rock weathering: field evidence and potential assessment in different humid regions. *Sci. Total. Environ.* **903**, 166118 (2023).

11. Wang, Z.Y., Teng, F. & Reiner, D.M. Assessing the potential and cost of enhanced rock weathering in China. *Commun. Earth Environ.* (2026).

12. Zhu, Q.C. et al. Cropland acidification increases risk of yield losses and food insecurity in China. *Environ. Pollut.* **256**, 113145 (2020).

13. Nie, L. & Peng, S. Chapter 2: Rice Production in China. In: Chauhan, B., Jabran, K., Mahajan, G. (eds) Rice Production Worldwide. *Springer, Cham* (2017).

14. Suhrhoff, T.J. et al. An ecosystem of carbon dioxide removal reviews – Part 3: Enhanced weathering [EB/OL]. *CDRXIV* (2026-07-16). https://doi.org/10.70212/cdrxiv.2026417.v1.

15. Kantola, I.B., Masters, M.D., Beerling, D.J., Long, S.P. & DeLucia, E.H. Potential of global croplands and bioenergy crops for climate change mitigation through deployment for enhanced weathering. *Biol. Lett.* **13**, 20160714 (2017).

16. Wang, Y. et al. Potential benefits of liming to acid soils on climate change mitigation and food security. *Glob. Change Biol.* **27**, 2807–2821 (2021).

17. Swoboda, P., Döring, T.F. & Hamer, M. Remineralizing soils? The agricultural usage of silicate rock powders: A review. *Sci. Total. Environ.* **807**, 150976 (2022).

18. Guo, F.X. et al. Crop productivity and soil inorganic carbon change mediated by enhanced rock weathering in farmland: a comparative field analysis of multi-agroclimatic regions in central China. *Agric. Syst.* **210**, 103691 (2023).

19. Hartmann, J. et al. Enhanced chemical weathering as a geoengineering strategy to reduce atmospheric carbon dioxide, supply nutrients, and mitigate ocean acidification. *Rev. Geophys.* **51**, 113–149 (2013).

20. Liao, G.T. et al. Nutrient use efficiency has decreased in southwest China since 2009 with increasing risk of nutrient excess. *Commun Earth Environ.* **4**, 388 (2023).

21. Xu, Z. et al. From Deficiency to Enrichment: Diverging soil phosphorus trajectories across China's croplands (1980–2018). *Glob. Change Biol.* **32**, e71004 (2026).
22. Beerling, D.J. et al. Enhanced weathering in the US Corn Belt delivers carbon removal with agronomic benefits. *Proc. Natl. Acad. Sci. U.S.A.* **121**(9), e2319436121 (2024).
23. Beerling, D.J. et al. Transforming US agriculture for carbon removal with enhanced weathering. *Nature* **638**, 425–434 (2025).
24. Kelland, M.E. et al. Increased yield and CO_2 sequestration potential with the C_4 cereal Sorghum bicolor cultivated in basaltic rock dust-amended agricultural soil. *Glob. Change Biol.* **26**, 3658–3676 (2020).
25. Dietzen, C., Harrison, R. & Michelsen-Correa, S. Effectiveness of enhanced mineral weathering as a carbon sequestration tool and alternative to agricultural lime: an incubation experiment. *Int. J. Greenh. Gas. Con.* **74**, 251–258 (2018).
26. Yue, Q. et al. Green manure rotation and application increase rice yield and soil carbon in the Yangtze River valley of China. *Pedosphere* **33**(4), 589–599 (2023).
27. McFarland, C.R., Huggins, D.R. & Koenig, R.T. Soil pH and implications for management: an introduction. *Washington State University Extension* (2015).
28. Wang, X. et al. Enhanced rock weathering boosts ecosystem multifunctionality via improving microbial networks complexity in a tropical forest plantation. *J. Environ. Manage.* **373**, 123477 (2025).
29. Liao, P. et al. Liming reduces nitrogen uptake from chemical fertilizer but increases that from straw in a double rice cropping system. *Soil. Till. Res.* **235**, 105873 (2024).
30. Ding, C.F. et al. Changes in the pH of paddy soils after flooding and drainage: modeling and validation. *Geoderma* **337**, 511–513 (2019).
31. Holland, J.E. et al. Yield responses of arable crops to liming – An evaluation of relationships between yields and soil pH from a long-term liming experiment. *Eur. J. Agron.* **105**, 176–188 (2019).
32. Suhrhoff, T.J. et al. Agricultural liming is a carbon sink in the Mississippi River Basin. *Nature* (2026).
33. Kanzaki, Y., Planavsky, N.J. & Reinhard, C.T. New estimates of the storage permanence and ocean co-benefits of enhanced rock weathering. *PNAS Nexus*, **2**(4), 1–9 (2023).
34. Guo, J.H. et al. Significant acidification in major Chinese croplands. *Science* **327**, 1008–1010 (2010).
35. Zhang, W. et al. Stabilization of acidification in China's cropland soils. *Nat. Geosci.* **18**, 1125–1132 (2025).
36. Sun, Y.M. et al. Decadal shifts in soil pH and organic matter differ between land uses in contrasting regions in China. *Sci. Total. Environ.* **740**, 139904 (2020).
37. Liao, P. et al. Liming reduces soil phosphorus availability but promotes yield and P uptake in a double rice cropping system. *J. Integr. Agr.* **19**(11), 2807–2814 (2020).
38. Liao, P. et al. Liming increases yield and reduces grain cadmium concentration in rice paddies: a meta-analysis. *Plant Soil* **465**, 157–169 (2021).
39. Zacharias, Q.C. et al. Spatiotemporal soil fertility responses to enhanced rock weathering along a hillslope catena within a temperate, agricultural watershed. *Nutr. Cycl. Agroecosyst.* **132**, 25 (2026).
40. Moretti, L.G. et al. Dunite in agriculture: physiological changes, nutritional status and soybean yield. *Commun. Soil Sci. Plan.* **50**(14), 1775–1784 (2019).
41. Silva, B., Paradelo, R., Vázquez, N., García-Rodeja, E. & Barral, M.T. Effect of the addition of granitic powder to an acidic soil from Galicia (NW Spain) in comparison with lime. *Environ. Earth Sci.* **68**, 429–437 (2013).
42. Yan, Y.X. et al. Wollastonite addition stimulates soil organic carbon mineralization: Evidences from 12 land-use types in subtropical China. *Catena* **225**, 107031 (2023).
43. Wang, F. et al. Wollastonite powder application increases rice yield and CO_2 sequestration in a paddy field in Northeast China. *Plant Soil* **502**, 589–603 (2024).

44. Gong, X.L. et al. Investigating the effects of co-applied basalt and biochar on carbon removal efficiency and grain yield in rice paddy. *J. Environ. Manage.* **405**, 129708 (2026).
45. Huang, L.H. et al. Interactive effects of pH, EC and nitrogen on yields and nutrient absorption of rice (Oryza sativa L.). *Agr. Water Manage.* **194**, 48–57 (2017).
46. Ishimaru, Y. et al. Mutational reconstructed ferric chelate reductase confers enhanced tolerance in rice to iron deficiency in calcareous soil. *Proc. Natl. Acad. Sci. U.S.A.* **104**(18), 7373–7378 (2007).
47. Saleem, A. et al. Alkaline and acidic soil constraints on iron accumulation by Rice cultivars in relation to several physio-biochemical parameters. *BMC Plant Biol.* **23**, 397 (2023).
48. Cong, L.H. et al. Harnessing enhanced rock weathering for carbon neutrality: potential and challenges in China. *Earth-Sci. Rev.* **271**, 105309 (2025).
49. Lefebvre, D. et al. Assessing the potential of soil carbonation and enhanced weathering through Life Cycle Assessment: a case study for Sao Paulo State, Brazil. *J. Clean. Prod.* **233**, 468–481 (2019).
50. Luo, Y.C. et al. Identifying the spatiotemporal changes of annual harvesting areas for three staple crops in China by integrating multi-data sources. *Environ. Res. Lett.* **15**, 074003 (2020).
51. Deng, X. et al. Exploring negative emission potential of biochar to achieve carbon neutrality goal in China. *Nat. Commun.* **15**, 1085 (2024).
52. Zhang, L. et al. Assessment of CO_2 mineral storage potential in the terrestrial basalts of China. *Fuel* **348**, 128602 (2023).
53. China Aggregates Association. 2024 China Sand and Gravel Industry Operation Report (2025). (In Chinese). https://www.zgss.org.cn/zixun/zhuti/17089.html
54. Ren, Z.J. et al. Declining demand and circular transition possibilities of sand, gravel and crushed stone in China. *Nat. Commun.* **16**, 9294 (2025).
55. Zhang, B.Q., Kroeger, J., Planavsky, N.J. & Yao, Y. Techno-economic and life cycle assessment of enhanced rock weathering: A case study from the Midwestern United States. *Environ. Sci. Technol.* **57**, 13828–13837 (2023).
56. van der Bauwhede, R., Muys, B., Vancampenhout, K. & Smolders, E. Accelerated weathering of silicate rock dusts predicts the slow-release liming in soils depending on rock mineralogy, soil acidity, and test methodology. *Geoderma* **441**, 116734 (2024).
57. Bertagni, M.B., Calabrese, S., Cipolla, G., Noto, L.V. & Porporato, A. Advancing enhanced weathering modeling in soils: critical comparison with experimental data. *J. Adv. Model. Earth. Sy.* **17**, e2024MS004224 (2025).
58. Gudbrandsson, S., Wolff-Boenisch, D., Gislason, S.R. & Oelkers, E.H. An experimental study of crystalline basalt dissolution from $2 \leq pH \leq 11$ and temperatures from 5 to 75°C. *Geochim. Cosmochim. Ac.* **75**(19), 5496–5509 (2011).
59. Zhang, S., Reinhard, C.T., Liu, S., Kanzaki, Y. & Planavsky, N.J. A framework for modeling carbon loss from rivers following terrestrial enhanced weathering. *Environ. Res. Lett.* **20**, 024014 (2025).
60. Kanzaki, Y., Chiaravalloti, I., Zhang, S., Planavsky, N. J. & Reinhard, C. T. In silico calculation of soil pH by SCEPTER v1.0. *Geosci. Model Dev.* **17**, 4515–4532 (2024).
61. Maher, K. The dependence of chemical weathering rates on fluid residence time. *Earth Planet. Sc. Lett.* **294**, 101–110 (2010).
62. Calabrese, S., Parolari, A.J. & Porporato, A. Hydrologic transport of dissolved inorganic carbon and its control on chemical weathering. *J. Geophys. Res. Earth Surf.* **122**, 2016–2032 (2017).
63. White, A.F. & Brantley, S.L. The effect of time on the weathering of silicate minerals: why do weathering rates differ in the laboratory and field? *Chem. Geol.* **202**(3–4), 479–506 (2003).
64. Murphy, B.W. Impact of soil organic matter on soil properties—a review with emphasis on Australian soils. *Soil. Res.* **53**, 605–635 (2015).

65. Helyar, K.R., Cregan, P.D. & Godyn, D.L. Soil acidity in New South Wales—current pH values and estimates of acidification rates. *Aust. J. Soil Res.* **28**, 523–537 (1990).

66. Maher, K., Rogers, B., Perzan, Z. & Kukla, T. Surface proton reservoirs constrain alkalinity export from enhanced weathering. *Environ. Sci. Technol.* **60**(34), 24044–24056 (2026).

67. DerSimonian, R. & Laird, N. Meta-analysis in clinical trials revisited. *Contemp. Clin. Trials* **45**, 139–145 (2015).

68. Hartung, J. & Knapp, G. A refined method for the meta-analysis of controlled clinical trials with binary outcome‡. *Statist. Med.* **20**, 3875–3889 (2001).

69. IntHout, J., Ioannidis, J.P. & Borm, G.F. The Hartung-Knapp-Sidik-Jonkman method for random effects meta-analysis is straightforward and considerably outperforms the standard DerSimonian-Laird method. *BMC Med. Res. Methodol.* **14**, 25 (2014).

70. Crippa, A. & Orsini, N. Multivariate Dose-Response Meta-Analysis: the dosresmeta R Package. *J. Stat. Softw.* **72**(1), 1–15 (2016).

71. Crippa, A. & Orsini, N. Dose-response meta-analysis of differences in means. *BMC Med. Res. Methodol.* **16**, 91 (2016).

72. Renforth, P. The potential of enhanced weathering in the UK. *Int. J. Greenh. Gas. Con.* **10**, 229–243 (2012).

73. Palandri, J.L. & Kharaka, Y.K. A compilation of rate parameters of water-mineral interaction kinetics for application to geochemical modeling. *U.S. Geological Survey, Menlo Park, CA* (2004).

74. te Pas, E.E.E.M., Chang, E., Marklein, A.R., Comans, R.N.J. & Hagens, M. Accounting for retarded weathering products in comparing methods for quantifying carbon dioxide removal in a short-term enhanced weathering study. *Front. Clim.* **6**,1524998 (2025).

75. McBride, A.L. et al. Quantifying potential carbon dioxide removal via enhanced weathering using porewater from a field trial in Scotland. *Front. Clim.* **7**, 1606574 (2025).

Supplementary Information

Enhanced weathering in China's acidic rice fields offers potential agronomic co-benefits

Li Tan[1,*], E. Isadora Falkson[1], Tim Jesper Suhrhoff[2,1], Christopher T. Reinhard[3], Noah J. Planavsky[1,2,*]

[1]Department of Earth and Planetary Sciences, Yale University, New Haven, CT 06511, USA.
[2]Yale Center for Natural Carbon Capture, Yale University, New Haven, CT 06511, USA.
[3]School of Earth and Atmospheric Sciences, Georgia Institute of Technology, Atlanta, GA 30332, USA.

Corresponding author: noah.planavsky@yale.edu; li.tan@yale.edu

The PDF file includes:

I. Supplementary Methods (*pp*.1–12)
II. Supplementary Tables 1 to 3 (*pp*.13–14)
III. Supplementary Figures 1 to 12 (*pp*.15–22)
IV. Supplementary References (*pp*. 23–26)

I. Supplementary Methods

Data collection and processing

Weathering kinetics are primarily controlled by the reactive surface area of the rock, application rate, soil properties (such as initial pH, bulk density, cation exchange capacity, etc.), and climate conditions, especially temperature and precipitation[1,2]. In general, finer particles, higher application rates, warmer and wetter conditions, and more acidic soils all promote faster dissolution[3,4]. For basalt-based Enhanced Weathering (EW) on cropland, fine particle sizes are commonly used to enhance dissolution, with many modeling and experimental studies considering *p*80 or equivalent fine powder size ranges of approximately 10–50 μm[5,6], although coarser settings, such as *p*80 = 100 μm, are also frequently evaluated[7]. Particle sizes below 10 μm can enhance Carbon Dioxide Removal (CDR) efficiency, but the gain is often outweighed by the substantial increases in grinding energy, dust generation, cost, and health risks due to inhalation[8]. Particle sizes greater than 100 μm substantially slow down dissolution, thereby affecting short-term impacts[9,10]. The grinding cost difference between 10–50 μm is minimal, and costs only begin to change markedly below roughly 10 μm[11]. Wang et al. also suggested that the 2–50 μm particle size range offers the most favorable balance between net carbon removal potential and economic costs. This advantage is particularly evident in basalt[12].

The basalt feedstock we use in our baseline case[13] originates from the Cascade Range in Oregon (Central Oregon Basalt Products LLC, Madras, Oregon, USA). The age is mid-Miocene, belonging to the "Prineville Chemical Type Unit" of the Columbia River basalts[14]. After screening and extraction, the particle size distribution of the processed basalt was measured using a LA-950 laser diffraction particle size analyzer (Horiba UK Ltd, Northampton, UK), showing a range of 1.5–300 μm and a *p*80 of 35 μm. The specific surface area (SSA) of the treated basalt was determined using an Anton Paar Nova 800 Brunauer Emmett Tell surface area analyzer at the Yale Geochemical Center and was 10.22 $m^2\ g^{-1}$, with an analytical error estimate of 0.01 $m^2\ g^{-1}$ based on five analyses. X-ray diffraction analysis also identified approximately 2.5% smectite in the basalt feedstock[13], which may influence the measured SSA, but this uncertainty was partially addressed through the reactive surface area sensitivity analysis.

The baseline case uses 50 t ha^{-1} per application in the 0–12 cm layer. An initial application is assigned in 2026, with additional applications considered in 2036, 2046, and 2056 only where modeled pH immediately before application remains < 6.5. This application rate falls within the range reported in field trials and other EW studies on cropland aimed at enhancing crop yield[15,16]. The use of pH 6.5 as an agronomically relevant acidity threshold is consistent with recent large-scale EW assessments, whereas the decadal reapplication interval is a scenario assumption[17]. The basalt application is assumed to be uniformly incorporated into the upper 0–12 cm of soil. This depth is treated as an effective shallow mixing layer. Agricultural EW studies and models use a range of surface soil incorporation depths (10–30 cm)[15,18,19], while cultivated rice soils are commonly disturbed within approximately the upper 10–20 cm[20]. We therefore use 12 cm as a representative shallow incorporation depth for the national-scale assessment. The characteristics of the feedstock are as shown in Supplementary Table 1. Additional chemical and structural information on the raw materials is provided by Kelland et al.[14] and Lewis et al.[21].

To quantify the yield response of Chinese rice to soil pH, we compiled a dedicated dataset relating rice yield to soil pH. We searched English and Chinese literature published from 2006 to

2025 through the Web of Science (WoS) and China National Knowledge Infrastructure (CNKI). Search terms included "yield," "rice," "paddy," "soil pH," and "China," as well as their corresponding Chinese characters, combined using AND/OR operators. Retrieved studies were screened using the following criteria: (1) field trials were conducted in mainland China; (2) matched soil pH and rice yield data were simultaneously available, with at least five paired observations to avoid potential biases from insufficient samples; (3) soil pH was acidic or weakly acidic (pH < 7.0); (4) the location and timing of the field experiment were reported; (5) to avoid duplicate results from the same site, if the soil pH data for a given location in the paper corresponded to yields from different years, we used the data from the latest year; (6) the soil environment was uncontaminated. For each selected study, raw data were obtained directly from tables when available, whereas data presented only in figures were digitized using Get Data Graph Digitizer. Ultimately, a total of 71 peer-reviewed papers were collected, providing 549 paired observations of soil pH and rice yield. These datasets are provided in Supplementary Data 1 and Supplementary Data 2, including information on author, publication date, title, soil pH, yield (direct observations), and relative yield normalized to highest within-study reported yield (RY).

For spatial processing, distributions of extracted acidic rice fields, soil properties, and climatic factors were resampled to 1 km resolution, and spatial correction and intersection were applied to align all grids in ArcGIS. The acidic rice sites and corresponding soil property datasets used for modeling are listed in Supplementary Data 3. Modeling and quantification were conducted in Python. We then summarized the simulated outputs using descriptive statistics, including means, standard deviations, distributions, provincial totals, and temporal trends, and visualized the results through spatial mapping, interpolation, and sensitivity analyses. For the relationship between pH and yield, random-effects meta-analysis and linear regression were used to quantify and examine the response of relative yield to soil pH. To estimate the pH response to rock powder addition in fields (see section below), in the baseline case, the basalt grain-surface dissolution rate (WR_{grain}) was set to 3×10^{-12} mol m^{-2} s^{-1}, soil buffering capacity multiplier (β_i) to 1.00, effective reactive surface area to 1.00, and decelerating weathering parameter (α) to 0.05 yr^{-1}, and annual topsoil alkalinity leaching fraction (f_{leach}) to 0.05. This main setting was used to generate the primary estimates of soil pH elevation (ΔpH), relative yield improvement (ΔRY), gross CDR, and comprehensive index of co-benefits (CIC). Alternative assumptions for β_i, effective reactive surface area, WR_{grain}, α, f_{leach}, feedstock CDR capacity, and CIC weighting were evaluated as sensitivity analyses.

Detailed Methods

Soil pH alkalization

Weathering occurs when H_2CO_3 in rainwater, formed by dissolution of atmospheric CO_2, reacts with silicate minerals in rocks and soils (equation (1)), consuming H^+ ions and releasing cations such as Ca^{2+} and Mg^{2+} into solution. The release of these cations increases the alkalinity of the soil solution, that is, its capacity to neutralize acids. The HCO_3^-, H_4SiO_4 and alkaline cations produced by weathering can be leached from soil and transported to the ocean for safe storage. Additional HCO_3^- may precipitate as carbonate minerals (equation (2))[22].

$$CaMgSi_2O_6+4CO_2+6H_2O \rightarrow Mg^{2+}+Ca^{2+}+4HCO_3^-+2H_4SiO_4 \quad (1)$$

$$Ca^{2+}+2HCO_3^- \rightarrow CaCO_3+CO_2+H_2O \quad (2)$$

(1) Mass of soil treated. We need the soil mass per hectare to convert any per hectare alkalinity into per kg soil units. We explicitly remove the gravel fraction $(1-g)$ so as not to overestimate the mass of reactive fine soil.

$$M_{soil} = A \cdot z \cdot P_b \cdot (1-g) \cdot 1000$$

where A represents the area of 1 hectare (10000 m^2); z is the treated depth (0.12 m); P_b is bulk density; g is gravel fraction; the factor 1000 converts Mg to kg; M_{soil} is kg soil ha^{-1}.

(2) Basalt alkalinity potential (ANC_{basalt}). Only the alkaline oxides CaO and MgO are credited toward liming equivalence (standard agronomic practice). We compute the maximum moles of H^+ that could be neutralized if the rock fully dissolves.

$$n_{eq,ha} = 2 \times 10^6 \sum_{i \in \{CaO, MaO\}} \frac{RW_i}{M_i}$$

$$ANC_{basalt,kg} = \frac{n_{eq,ha}}{M_{soil}} [mol\ H^+\ kg^{-1}]$$

where R is rock dose (50 t ha^{-1}); W_i is oxide mass fraction (CaO = 5.3%, MgO = 2.4%); M_i is molar mass (CaO 56.077 g mol^{-1}, MgO 40.304 g mol^{-1}); the factor 10^6 converts tonnes to grams; the factor 2 converts moles of oxide to equivalents of H^+ neutralized (two charge equivalents per oxide formula unit); $n_{eq,ha}$ is mol H^+ ha^{-1}; $ANC_{basalt,kg}$ is per kg soil potential (if fully dissolved).

(3) Soil pH buffering capacity β_i. We convert moles of neutralized acidity per kg soil into an estimated pH increase using the spatially explicit soil pH buffering capacity, β_i, defined here as the amount of acidity or alkalinity required to change soil pH by one unit. This parameter captures the soil's resistance to pH change when acid or base is added. The base relationship follows the Helyar–Murphy soil organic matter (SOM) and clay formulation, in which buffering contributions are assigned separately to SOM and clay[23,24]. The original relation is expressed for a 10 cm layer and was scaled to the modeled 12 cm layer.

$$BC_{10,i} = 0.05\ (4.2 \cdot \%SOM + 2.0 \cdot \%Clay)$$

$$BC_{12,i} = BC_{10,i} \times \frac{12}{10}$$

$$\beta_i = \frac{BC_{12,i} \times 10^6}{M_{CaCO_3}} \times \frac{2}{M_{soil,i}}$$

$$\%SOM = 1.724 \times \%SOC$$

Where $BC_{10,i}$ and $BC_{12,i}$ represent the $CaCO_3$ equivalent buffering requirements (t $CaCO_3$ ha^{-1} pH^{-1}) for 10 and 12 cm soil layers, respectively; M_{CaCO_3} = 100.087 g mol^{-1}; $M_{soil,i}$ is from step (1), and 4.2 and 2.0 are the compound-specific BC values reported by Murphy[23]; %SOM equals 1.724 × %SOC using the conventional van Bemmelen conversion[25]; The factor 10^6 converts t to g, and each mole of $CaCO_3$ neutralizes two moles of H^+. We constrain $\beta_i \in [0.02, 1.50]$ to avoid nonphysical extremes, which is consistent with published ranges for sandy, low SOM soils at the low end, and organic/2:1 clay-rich soils at the high end[26], and uncertainty in β_i was evaluated using 0.75× and 1.25× sensitivity cases.

(4) Weathering kinetics. We consider climate as a sensitive background factor and describe an idealized dissolution process, ignoring changes in grain surface during dissolution[9,27]. We did not

explicitly simulate changes in grain geometry or shrinking-core evolution, but instead used measured SSA as an initial effective surface area parameter, while long-term field attenuation was represented by the decelerating weathering function and reactive surface area sensitivity analysis.

First-year dissolved fraction d:

$$d = SSA \times WR_{grain} \times \bar{M} \times t \cdot f_T \cdot f_P$$

$$f_T = \exp\left[-\frac{E_a}{R_g}\left(\frac{1}{T_K} - \frac{1}{T_{ref}}\right)\right]$$

$$f_P = \min\left[1.5, \max\left(0.5, \frac{P}{1000}\right)\right]$$

where SSA is specific surface area (10.22 m^2 g^{-1}); WR_{grain} represents basalt grain-surface dissolution rate; $\bar{M}$ is effective molar mass of basalt (125 g mol^{-1})[28]; t is seconds per year; f_T is temperature factor and f_P is precipitation factor. These factors scale the first-year basalt dissolved fraction according to local climatic conditions; T_K is annual mean temperature in kelvin; R_g is the gas constant. We bound d between 0.002–0.20 yr^{-1}. Temperature dependence is represented by an Arrhenius factor with E_a = 50 kJ mol^{-1} and T_{ref} = 293.15 K, while precipitation is represented by the bounded scalar f_P = P/1000 constrained to 0.5–1.5. The precipitation term is a regional screening parameterization rather than a mechanistic soil and water balance[29,30]. Field rates decline with time due to surface armoring, secondary coatings, and the most reactive materials at the surface (relative to less reactive/slower to react materials). The decelerating curve is a simple, smooth way to embody that trend (consistent with the time-dependent rate decline discussed by White & Brantley)[28].

Cumulative dissolved fraction $F(t)$:

Decelerating (DL): $F_{DL}(t) = 1 - (1 + \alpha t)^{-(d/\alpha)}$ (empirical passivation)

(5) Annual alkalinity retention, leaching, and ΔpH. For each basalt cohort, newly released alkalinity was calculated from the annual increment in the cumulative dissolved fraction. The retained topsoil stock was then updated recursively so that the annual leaching fraction acted on both previously retained alkalinity and newly released alkalinity.

$$\Delta F_i(a) = F_{DL,i}(a) - F_{DL,i}(a-1)$$

$$G_i(0) = 0$$

$$G_i(a) = [G_i(a-1) + \Delta F_i(a)](1 - f_{leach})$$

$$A_{ret,i}(t) = ANC_{basalt,i} \sum_{c \in C,\, t > y_c} I_{i,c}\, G_i(t - y_c)$$

$$\Delta pH_i(t) = \frac{A_{ret,i}(t)}{\beta_i}$$

$$I_{i,2026} = 1; \qquad I_{i,c} = 1[pH_i(c^-) < 6.5], \quad c \in \{2036, 2046, 2056\}$$

where a is cohort age in years; $\Delta F_i(a)$ is the fraction newly dissolved during year a; $G_i(a)$ represents the fraction of one cohort's weathering-derived alkalinity retained in the modeled topsoil after annual leaching; f_{leach} is the annual leaching fraction; c is the set of possible application cohorts; y_c is the application year of cohort c, and $I_{i,c}$ indicates whether that cohort was actually applied. The reference value used f_{leach} = 0.05, with 0.02 and 0.10 tested as sensitivity cases. These fractions are screening assumptions used to represent uncertain topsoil export rather than universal measured constants. Recent experiments and reactive transport analyses show that weathering products may be retained on soil surfaces or within the profile before hydrological

export, supporting explicit separation of retained and exported alkalinity[31,32]. The 2026 cohort was applied to all modeled sites; in 2036, 2046, and 2056, another 50 t ha^{-1} cohort was applied only if modeled pH immediately before application remained < 6.5[17]. Contributions from all applied cohorts were summed.

For regional scale screening, we treated β_i as a local linear approximation of soil pH buffering capacity for each grid cell. We reduce the risk of over- or under-shooting by anchoring β_i to SOM and clay, as pH buffering capacity can be estimated from SOM, clay/mineral characteristics, and exchange properties[33,34,35]. Over large pH changes pH buffering can be nonlinear; accordingly, the single β_i approach should be interpreted as a first-order approximation rather than a full titration curve model[26]. We therefore evaluated the influence of this assumption using sensitivity cases.

(6) Main weathering parameter setting. From laboratory and compilation studies on basaltic glass and basalts at near-neutral pH and ~20–25 °C, far from equilibrium rates often fall in a band around 10^{-13}–10^{-11} mol m^{-2} s^{-1}, depending on mineralogy and conditions[29,30]. Considering the fine particle size and measured SSA of the basalt used here, we used WR_{grain} = 3 × 10^{-12} mol m^{-2} s^{-1} as the main basalt grain-surface dissolution rate, representing a moderately reactive and realistic weathering condition. The measured SSA was fixed at 10.22 m^2 g^{-1}, and the decelerating dissolution parameter was set to α = 0.05 yr^{-1} to represent progressive field-scale rate decline associated with processes such as surface evolution, secondary coatings, transport limitation, and passivation[28].

Rice yield improvement

(1) Data extraction and standardization. To make yield values comparable across papers with different yield units, cultivars, sites, and years, we standardized yield within each paper to relative yield.

$$RY_{ij} = \frac{Y_{ij}}{max_j\left(Y_{ij}\right)}$$

where i refers paper i; j represents observation index within paper i; Y_{ij} denotes the rice yield for observation j in paper i; $max_j\left(Y_{ij}\right)$ reflects the maximum yield among all extracted observations within paper i; RY_{ij} represents relative yield ∈ (0,1].

(2) Study overview and the slope of RY corresponding to soil pH within each paper. We plotted a within-paper linear fit and an overall control group (CK) by linear regression to outline the heterogeneity and direction of relationships across studies. Then, we estimated the slope of RY corresponding to soil pH within each paper. To derive a response function applicable to our scenario calculations, we estimated within-study soil pH–relative yield slopes using only observations with pH in [4.5,7.0] to avoid bias from very acidic outliers. One study has only two points in [4.5,7.0]; thus, slope standard error (SE) cannot be estimated and the study is excluded from inverse variance pooling. For each paper i, fit:

$$RY_{ij} = a_i + b_i \cdot pH_{ij} + e_{ij}$$

where a_i reflects intercept for paper i; pH_{ij} represents the soil pH value for observation j in paper i; b_i terms slope for paper i (change in relative yield per 1-unit increase in pH); e_{ij} refers residual (error term) for observation j in paper i.

(3) Random-effects meta-analysis of ΔRY across papers. We acknowledge that true effects vary across studies due to different soils, varieties, amendments, and other environmental conditions. Random-effects pooling is a standard approach for heterogeneous datasets (see the Methods) and

inverse variance weighting is a standard framework for pooling estimated effects[36,37]. Between-study variance was estimated using DerSimonian–Laird, a classic random-effects estimator. Uncertainty for the pooled effect was evaluated using the Hartung–Knapp refinement[38,39]. Therefore, we pool the 70 usable b_i values using an inverse variance random-effects meta-analysis (DerSimonian–Laird), then estimate the RY per 0.1-unit increase in pH ($\Delta RY_{0.1}$):

$$\text{Study weights: } w_i = \frac{1}{SE(b_i)^2 + \tau^2}$$

$$\text{Pooled slope: } b_{pooled} = \frac{\sum_i w_i b_i}{\sum_i w_i}$$

$$\Delta RY_{0.1} = 0.1 \times b_{pooled}$$

where $SE(b_i)$ is slope standard error in paper i; $SE(b_i)^2$ is within-paper variance; τ^2 represents between-paper variance (heterogeneity). We plot a forest figure that includes effect, SE, weight of each study, and final results, as shown in Supplementary Fig. 5.

(4) Robustness check. To demonstrate that the main coefficient is not an artifact of the selected pH range, we repeated the above method using all extracted observations, including points with pH < 4.5. The resulting response coefficient is 0.0121 per 0.1-unit pH increase, with a 95% confidence interval (CI) of 0.0080–0.0163 and heterogeneity (I^2) ≈ 77.4%. This coefficient was slightly higher than the main estimate, which is expected because extremely acidic soils often show stronger yield recovery per unit pH increase. Therefore, the main coefficient derived from the pH 4.5–7.0 range was retained for scenario calculation because it better matched the calibration range used for yield-benefit estimation. As an additional check for the descriptive CK regression, we also repeated the linear fit after excluding observations with pH < 4.5, which matches the calibration range used for yield benefit estimation. The relationship remains positive but weakens (slope = 0.0584, R^2 = 0.08), confirming that the full range regression is partly influenced by the extreme acidic observation. Therefore, CK regression is interpreted only as supporting descriptive evidence for the positive tendency of pH and yield under standard practice, while the yield benefit calculation is based on the random-effects meta-analysis rather than this simple regression.

(5) Diminishing returns. Agronomically, diminishing returns are expected. Yield gains from raising pH are typically largest when soils are strongly acidic, and they taper as pH approaches a near-optimal range[40]. To quantify diminishing returns, we estimated a fractional logit model with paper fixed effects[41] and computed the average marginal growth in predicted RY per 0.1-unit increase in pH. Specifically, for each observation we calculated $\Delta\widehat{RY}_{0.1} = \widehat{RY}(pH + 0.1) - \widehat{RY}(pH)$, then averaged $\Delta\widehat{RY}_{0.1}$ within 0.5-pH bins over pH 4.5–7.0. The resulting bin-wise marginal effects decline with increasing pH, indicating that diminishing returns are consistent with known crop pH response behavior[40].

$$\Delta pH_{eff,i,t} = \min\left[\max\left(\Delta pH_{i,t}, 0\right), \max\left(0, 7.0 - pH_{0,i}\right)\right]$$

$$\Delta \mathrm{RY_{i,t}}(\%) = \frac{1}{0.1}\int_{\mathrm{pH_{0,i}}}^{\mathrm{pH_{0,i}} + \Delta \mathrm{pH_{eff,i,t}}} k(\mathrm{pH})\ \mathrm{d\ pH}$$

where $\Delta pH_{i,t}$ represents the modeled soil pH increase for grid cell i at time t; $pH_{0,i}$ is the initial soil pH before the first basalt application; $\Delta pH_{eff,i,t}$ is constrained to be non-negative and capped at the increase required to reach pH 7.0; d pH denotes an infinitesimal increment in soil pH over which the yield response is integrated; $k(pH)$ is the RY response coefficient for each pH interval crossed, expressed in percentage points per 0.1-unit increase in pH. The coefficients are 1.23 for 4.5

≤ pH < 5.0, 1.03 for 5.0 ≤ pH < 5.5, 0.86 for 5.5 ≤ pH < 6.0, 0.73 for 6.0 ≤ pH < 6.5, and 0.54 for 6.5 ≤ pH < 7.0. The integral sums these specific interval contributions, allowing the marginal response to decrease as pH rises. Yield improvement is evaluated relative to the original pH at each time point, rather than accumulated across years. No additional positive benefit is assigned above pH 7.0. Modeled ΔpH is retained at full numerical precision, with rounding applied only to reported results.

Carbon dioxide removal capacity

(1) Stoichiometric CO_2 removal capacity of basalt. We use standard EW stoichiometry from Renforth[42] and later work[7,43], according to which the gross CO_2 capacity depends on CaO and MgO contents.

$$R_{CO_2,max} = \frac{M_{CO_2}}{100}\left(\alpha\frac{CaO}{M_{CaO}} + \beta\frac{MgO}{M_{MgO}}\right)\eta$$

$$CDR_{max,ha} = R_{app} \cdot R_{CO_2,max} = 50 \times 0.1356 \approx 6.78\ t\ CO_2\ ha^{-1}$$

where $R_{CO_2,max}$ represents the ideal gross feedstock CO_2 capacity in t CO_2 t^{-1} basalt if all CaO and MgO weather with atmospheric CO_2; CaO and MgO are the weight percentages in basalt (5.3 and 2.4 respectively, see Supplementary Table 1); M_{CO_2} is molar mass of CO_2 (44.01 g mol^{-1}); M_{CaO} is molar masses of CaO (56.08 g mol^{-1}); M_{MgO} is molar masses of MgO (40.30 g mol^{-1}); α and β describe the contributions of CaO and MgO, while η is the molar ratio of CO_2 uptake to divalent-cation release. For fully reactive CaO and MgO, α=β=1 and ideal bicarbonate-forming weathering gives η=2[43].

For the basalt composition used in this study, $R_{CO_2,max}$ equals approximately 0.1356 t CO_2 t^{-1} basalt. With a per-application rate of 50 t basalt ha^{-1}, the ideal gross full weathering capacity is therefore 6.78 t CO_2 ha^{-1} (ignoring Na/K and extra ocean alkalinity amplification).

(2) Shared dissolved fraction for ΔpH and CDR. To ensure internal consistency between soil alkalization and CDR accounting, the same cumulative decelerating basalt dissolved fraction for each applied cohort used for ΔpH estimation is also used to estimate gross CDR. For each grid cell i and time horizon t, the cumulative dissolved fraction is calculated as:

$$F_{DL,i}(t) = 1 - (1 + \alpha t)^{-(d_i/\alpha)}$$

where $F_{DL,i}(t)$ is the cumulative fraction of basalt dissolved by time t, d_i represents the first-year dissolved fraction derived from the basalt grain-surface dissolution rate, measured specific surface area, temperature, and precipitation, and α is the passivation parameter. Because applications could occur in 2026, 2036, 2046, and 2056, the dissolved fraction was:

$$F_{\Sigma,i}(t) = \sum_{c\in C,\, t>y_c} I_{i,c}\, F_{DL,i}(t - y_c)$$

where c is the set of possible application cohorts, y_c is the application year, and $I_{i,c}$ is the pH-based application indicator defined in the soil pH model. Thus, $F_{\Sigma,i}(t)$ can exceed 1 after multiple 50 t ha^{-1} cohorts because it is the sum of dissolved fractions across independent applications, not the fraction dissolved from a single dose.

(3) For each grid cell, gross CDR is calculated as:

$$CDR_i^{gross}(t) = A_i \times 100 \times CDR_{max,ha} \times F_{\Sigma,i}(t)$$

where $CDR_i^{gross}(t)$ represents the gross CDR in grid cell i at time horizon t; A_i is the grid cell area in km^2; 100 converts km^2 to ha; $CDR_{max,ha}$ is the ideal gross feedstock CO_2 capacity in step

(1); and $F_{\Sigma,i}(t)$ is defined in step (2). Total gross CDR is then obtained by summing CDR_i^{gross} across all grid cells:

$$CDR^{gross}(t) = \sum_i CDR_i^{gross}(t)$$

These values represent gross chemical CDR from basalt weathering, not net CDR of life cycle assessment (LCA) or soil greenhouse gas (GHG) corrections, and we acknowledge that LCA and soil GHG would reduce net CDR, depending on rock type, source, and transport conditions[44]. This also follows the land area scaling used in large-scale EW assessments[6,7,45].

(4) Leached alkalinity CDR equivalent. In natural systems, weathering products may either remain within the soil profile or be exported in drainage. To account for this, we separately estimated the CDR equivalent associated with leached alkalinity, consistent with approaches that distinguish between weathering products retained in the soil and aqueous alkalinity export[31,32,46]. For one cohort, the cumulative leached fraction is the difference between the cumulative dissolved fraction and the retained alkalinity fraction:

$$F_{leach,i}(t) = \sum_{c \in C,\, t > y_c} I_{i,c}\left[F_{DL,i}(t - y_c) - G_i(t - y_c)\right]$$

$$CDR_i^{leach}(t) = A_i \times 100 \times R_{app} \times R_{CO_2,max} \times F_{leach,i}(t)$$

where $F_{\mathrm{leach},i}(t)$ is the cumulative fraction of weathering-derived alkalinity that has been leached from the modeled topsoil in grid cell i by time t. For each applied basalt cohort c, this fraction was calculated as the difference between the cumulative dissolved fraction, $F_{DL,i}$, and the fraction of weathering-derived alkalinity retained in the 0–12 cm soil layer after annual leaching, G_i. $I_{i,c}$ indicates whether cohort c was applied, and $t - y_c$ represents its age. The leached alkalinity CDR equivalent was then calculated from the cumulative leached fraction, grid cell area A_i, basalt application rate R_{app}, and maximum stoichiometric CO_2 removal capacity $R_{\mathrm{CO_2,max}}$. This quantity was treated as a secondary measurement, reporting, and verification (MRV) metric and was not added to gross CDR based on weathering.

Comprehensive index of co-benefits

To integrate the major EW co-benefits into a single comparative metric, we constructed the CIC based on ΔpH, ΔRY, and weathering-based gross CDR, representing the different dimensions of soil amelioration, agronomic response, and climate mitigation, respectively. Although ΔRY and CDR are the most direct agronomic and climate-related benefits, ΔpH is retained as an independent CIC component because it also represents a broader soil quality and environmental safety benefit. In acidic agricultural soils, increasing pH can reduce the mobility and bioavailability of many trace-metal cations, especially Cd and Pb, thereby potentially lowering crop uptake and food safety risks. Meta-analyses have shown that liming increases soil pH while reducing Cd accumulation in crops and rice grain[47,48]. This benefit may be particularly relevant for acidic rice fields in southern China, where soil acidification and heavy metal risks can coexist. The mobility of arsenic in flooded paddy soils is strongly controlled by redox conditions and Fe/Mn oxide cycling[49,50], rather than by pH alone. In addition, pH adjustment may influence non-CO_2 greenhouse gas emissions, as soil pH can regulate denitrification and N_2O production, and liming has been reported to reduce CH_4 and N_2O emissions in rice systems[51,52]. Therefore, ΔpH is not treated only as an intermediate driver of yield response, but also as an independent indicator of soil acidification mitigation and potential

environmental risk reduction.

To address the differences in units and interpretation of these indicators, they were first aggregated at the provincial level and then normalized before index construction, following general recommendations for the development of composite indicators[53]. Soil pH elevation and relative yield improvement were represented by provincial mean ΔpH and provincial mean ΔRY, respectively, because both are intensive response indicators. In contrast, CDR was represented by cumulative provincial gross CDR because it is an extensive quantity expressed in mass units and can be summed across grid cells.

For each province and time horizon, the provincial mean ΔpH, provincial mean ΔRY, and cumulative gross CDR were calculated from the grid cell results. These three indicators were then normalized across provinces within the same time horizon using min–max normalization, which converted indicators with different units to a common dimensionless scale before aggregation. The provincial CIC was calculated as the weighted sum of the three normalized indicators. In the baseline case, equal weights were assigned to ΔpH, ΔRY, and CDR. This equal weight setting avoids imposing a prior preference among soil improvement, agronomic benefit, and climate mitigation. The provincial CIC was used to compare the relative suitability and co-benefit potential of EW deployment among provinces.

To evaluate the national temporal trend in comprehensive co-benefits, we also calculated an overall CIC for each time horizon. National mean ΔpH, national mean ΔRY, and national cumulative gross CDR were calculated from the provincial results. These indicators were normalized relative to their maximum values across each of the time horizons, and the overall CIC was calculated using the same weighting structure as the provincial CIC. This approach provides a direct comparison of how the overall co-benefit potential changes from 2030 to 2060. The robustness of provincial prioritization was evaluated using alternative CIC weights, as described in the following section of this document.

Potential economic benefits

To provide a preliminary assessment of the economic benefits associated with EW-induced rice yield improvement, we estimated the additional rice production and corresponding revenue based on the modeled yield responses, acidic rice field area, national average rice yield, and rice purchase price. The mean yield improvement over 2026–2060 was estimated by linear interpolation between the modeled reporting years (2030, 2040, 2050, and 2060), assuming zero improvement at the beginning of 2026, yielding an average of 5.46%. China's national average rice yield was 7.21 t ha^{-1} in 2025 (National Bureau of Statistics of China. https://www.stats.gov.cn/english/PressRelease/202512/t20251215_1962079.html). A representative rice procurement price of CNY 2,647 t^{-1} was estimated from the average purchase prices of early indica, middle/late indica, and japonica rice reported in December 2025 (Shanghai National Grain Trading Center. https://www.shyouandme.com/fenxiyuce/124989.htm), corresponding to approximately USD 368.32 t^{-1} using the 2025 average exchange rate of CNY 7.1875 per USD (Federal Reserve Board. https://www.federalreserve.gov/releases/g5a/current). The annualized gross economic benefit and cumulative economic benefit were estimated as follows:

$$B_{annual} = A \times Y_0 \times \overline{\Delta RY} \times P$$

$$B_{total} = B_{annual} \times T$$

$$B_{CDR} = \frac{B_{total}}{CDR_{total}}$$

where B_{annual} is the estimated annualized gross rice revenue benefit (USD yr^{-1}); A is the area of acidic rice fields (24.54×10^6 ha); Y_0 is the baseline rice yield (7.21 t ha^{-1}); the $\overline{\Delta RY}$ over 2026–2060 is 0.0546; P is the representative rice procurement price (USD 368.32 t^{-1}); T is the assessment period (35 years); B_{total} is the cumulative gross revenue benefit (USD); CDR_{total} is the modeled cumulative gross CDR (204.39×10^6 t CO_2); and B_{CDR} is the additional agricultural revenue benefit per tonne of gross CDR (USD t^{-1} CO_2).

This calculation assumes that the modeled changes in normalized relative yield correspond to proportional increases in physical rice production, and that the assessed field area represents annually harvested rice area. Because ΔRY represents percentage point changes in normalized relative yield, the actual proportional yield increase depends on the initial RY and may be higher than assumed here. Baseline yield, rice prices, and cultivated area were held constant, and deployment costs, future market changes, and discounting were not considered. Therefore, the results represent illustrative gross economic benefits rather than net economic returns.

Sensitivity analysis

(1) Weathering, soil buffering, and alkalinity-leaching sensitivity. To evaluate the robustness of the modeled co-benefits to key parameter assumptions, we conducted a sensitivity analysis for five parameters that directly control basalt dissolution or soil pH response: β_i, effective reactive surface area, WR_{grain}, α, and f_{leach}. These parameters were selected because mineral dissolution rates are strongly affected by reactive surface area, mineral reactivity, temperature, hydrological conditions, and reaction progress[29,30], while field weathering rates commonly decline over time because of surface evolution, secondary coatings, transport limitation, and passivation[28]. Soil pH buffering was included because the conversion of released alkalinity into change in pH depends strongly on SOM, clay minerals, and exchange properties[29,34,35]. Annual alkalinity leaching was included because weathering-derived alkalinity can be retained within soil or exported hydrologically, affecting the alkalinity stock available for pH neutralization[31,32]. Sensitivity cases were calculated by changing one parameter setting at a time while keeping all other parameters identical to the baseline case. The same equations described above for the first-year dissolved fraction, cumulative decelerating dissolved fraction, soil pH elevation, and gross CDR were used in all cases. The parameter settings are summarized in Supplementary Table 2.

(2) CDR feedstock sensitivity. We evaluated the sensitivity of gross CDR to feedstock CaO and MgO contents. The baseline case used the measured composition of basalt, with CaO = 5.3% and MgO = 2.4%, yielding an ideal gross feedstock CO_2 capacity of $R_{CO_2,max}$ = 0.1356 t CO_2 t^{-1} basalt. However, national basalt data indicate that Chinese basalts contain higher average CaO and MgO contents; thus, we added a feedstock sensitivity using CaO = 9.10% and MgO = 7.35%[54], as shown in Supplementary Table 3. In this case, $R_{CO_2,max}$ was recalculated while keeping the same modeled cumulative dissolved fraction $F_{DL,i}(t)$, application rate, and grid cell area as in the baseline case. This sensitivity analysis was used only to evaluate the effect of feedstock chemistry on gross CDR capacity and was not treated as a separate soil alkalization or yield scenario.

(3) CIC weighting sensitivity. Because weighting choices can influence composite indicator values and rankings, we conducted a CIC weighting sensitivity analysis to evaluate whether

provincial prioritization was robust under alternative benefit weight assumptions[55,56]. This analysis did not change the underlying ΔpH, ΔRY, or CDR results, but recalculated the CIC by applying alternative weights to the same normalized indicators. Three weighting schemes were tested: soil pH priority, rice yield priority, and CDR priority. The target indicator was assigned a weight of 0.50, while the other two indicators were each assigned a weight of 0.25. These schemes were used to test whether provincial CIC rankings were sensitive to stronger emphasis on soil improvement, agronomic benefit, or climate mitigation. Provincial CIC rankings and overall CIC trends were compared across the weighting schemes.

Model evaluation through sensitivity analysis and literature comparison

We plotted the temporal evolution of mean cumulative basalt dissolution under different weathering assumptions. Mean cumulative basalt dissolution increased throughout 2030 to 2060, with the baseline case rising from approximately 0.39 to 1.23 and showing a slower increase after 2040 (Supplementary Fig. 4). Within the tested ranges, cumulative basalt dissolution was more sensitive to reactive surface area and WR_{grain} than to the attenuation coefficient, highlighting the importance of constraining these parameters under field conditions. Under adaptive reapplication, continued dissolution across successive basalt cohorts can support further gross CDR even as topsoil pH benefits weaken, because modeled pH depends on the balance between alkalinity release and export.

To place the weathering and CDR assumptions of our reference model in context, we compared the selected WR_{grain} value and the area-normalized CDR estimates with published laboratory, field, and column-based EW values (Supplementary Fig. 12). The weathering rate comparison shows that the main value used (3×10^{-12} mol m^{-2} s^{-1}) is lower than basaltic glass dissolution rates[29], as this report was based on a pH of 4.0, whereas the average pH in our study area was 5.96, with a minimum pH of 4.5. Compared with dissolution rates corresponding to our pH range, this rate overlaps with the lower range of crystalline basalt dissolution rates (pH 4.0–6.5)[57], and is higher than some compiled plagioclase/feldspar rates (pH 5.1–7.0)[58]. Therefore, the selected value is reasonable as an effective weathering rate parameter for field-scale EW screening. After normalization by treated area and assessment duration, the baseline case gives an average annualized gross CDR rate of 0.2380 t CO_2 ha^{-1} yr^{-1} over 35 years, compared to 0.5308 t CO_2 ha^{-1} yr^{-1} for the first 5 years. These values are higher than the lower-to-middle range of published basalt EW estimates[59], which span from approximately 0.01–0.4 t CO_2 ha^{-1} yr^{-1} to high estimates of about 2.24–2.6 t CO_2 ha^{-1} yr^{-1} (Supplementary Fig. 12). These rates are difficult to compare directly, as application rates, basalt composition, climatic conditions, and quantification methods all result in significant variations in CDR rate. For example, the CDR rate of 2.6 t CO_2 ha^{-1} yr^{-1} is an estimate based on an annual application of 50 t ha^{-1} [15], while 2.24 t CO_2 ha^{-1} yr^{-1} represents a short-term potential over a 235-day cycle[13]. Regardless, we assert that additional sensitivity tests beyond our baseline case should largely account for field-scale attenuation of basalt dissolution. Therefore, although the results are reported as gross rather than net LCA-adjusted CDR rates, we do not expect them to be based on an unconstrained maximum weathering assumption.

We minimized reliance on poorly constrained assumptions where available data did not support more detailed process representation. For SSA, we used a decelerating dissolution function to provide a transparent effective surface area parameterization suitable for national scale screening.

Although a shrinking core model can be used to represent particle size reduction during dissolution, it would require additional assumptions about grain geometry, mineral-specific dissolution, and the evolution of surface accessibility that are poorly constrained at the national scale. Our approach instead accounts for long-term decline in field rate through the deceleration parameter α and reactive surface area sensitivity cases[11,28,59].

II. Supplementary Tables

Supplementary Table 1 | Basalt characteristics and deployment parameters.

Particle diameter	$p80$ = 35 μm
SSA	10.22 m^2/g ± 0.01 m^2/g
Application rate	50 t ha^{-1} per application
Application timing	2026 initial application; conditional reapplications in 2036, 2046, and 2056 when modeled pre-application pH < 6.5
Treated layer	0-12 cm
CaO	5.30%
MgO	2.40%
Na_2O	3.80%
K_2O	3.00%
TiO_2	2.40%
Al_2O_3	13.00%
P_2O_5	2.30%
FeO	9.70%
SiO_2	44.30%

Supplementary Table 2 | Weathering, soil buffering, and alkalinity leaching parameter settings of sensitivity analysis.

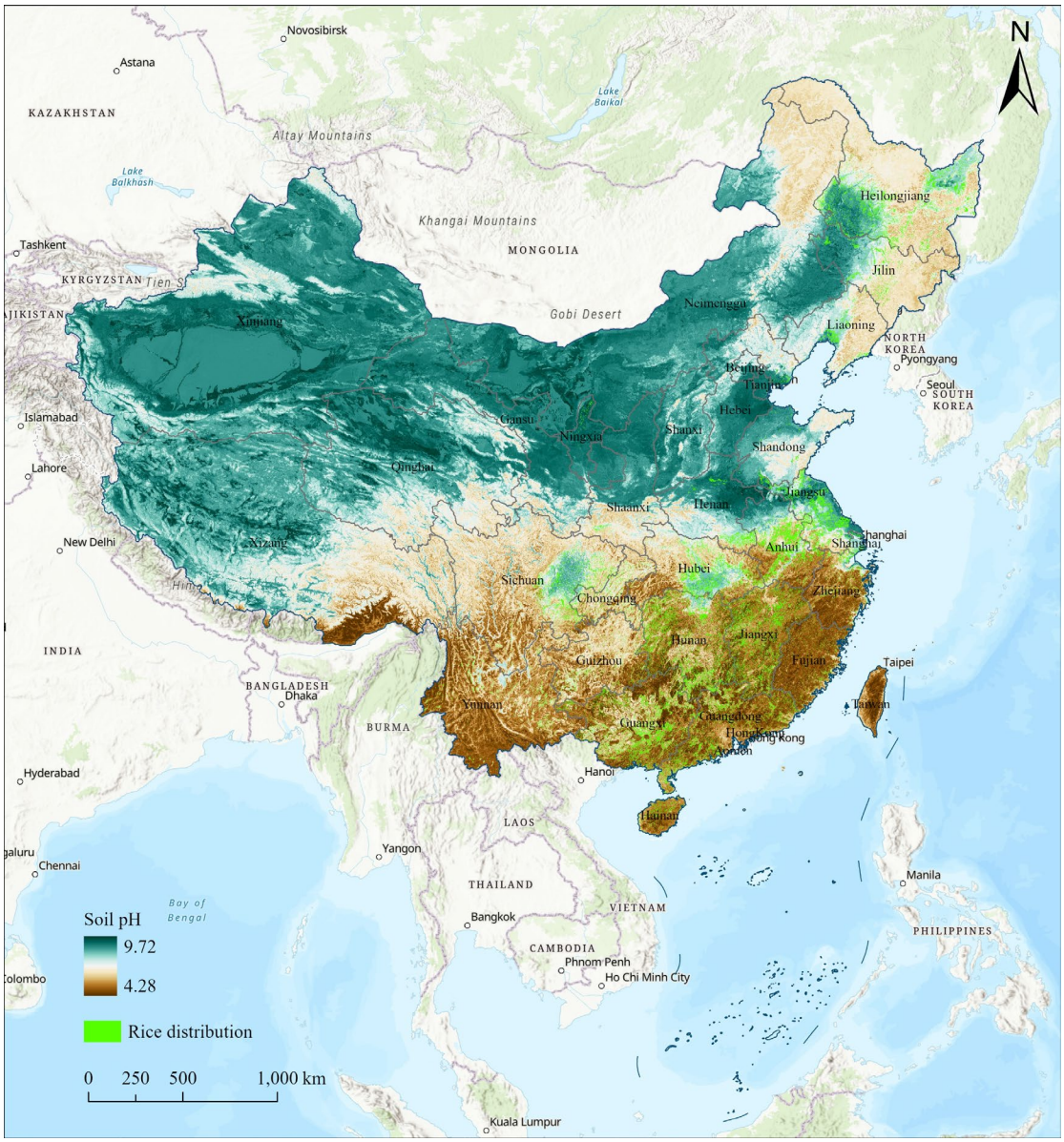
Parameter	Reference value	Sensitivity settings	Main affected assessments	Rationale
Soil buffering capacity, β_i	Spatially explicit β_i ($f_\beta = 1.00$)	0.75 β_i, 1.25 β_i	ΔpH, ΔRY	Tests uncertainty in converting released alkalinity into pH change
Effective reactive surface area	1.00 × SSA	0.50 × SSA, 1.50 × SSA	ΔpH, ΔRY, CDR	Tests uncertainty in accessible field reaction surface area
WR_{grain}	3 × 10^{-12} mol m^{-2} s^{-1}	1 × 10^{-12} mol m^{-2} s^{-1}, 5 × 10^{-12} mol m^{-2} s^{-1}	ΔpH, ΔRY, CDR	Tests uncertainty in basalt reactivity
Passivation	0.05 yr^{-1}	0.03 yr^{-1}, 0.10 yr^{-1}	ΔpH, ΔRY, CDR	Tests weaker or

Parameter	Reference value	Sensitivity settings	Main affected assessments	Rationale
parameter, α				stronger long-term rate decline
Annual topsoil alkalinity leaching fraction, f_{leach}	0.05 yr^{-1}	0.02 yr^{-1}, 0.10 yr^{-1}	ΔpH, ΔRY	Tests uncertainty in annual loss of weathering-derived alkalinity retained in the modeled topsoil

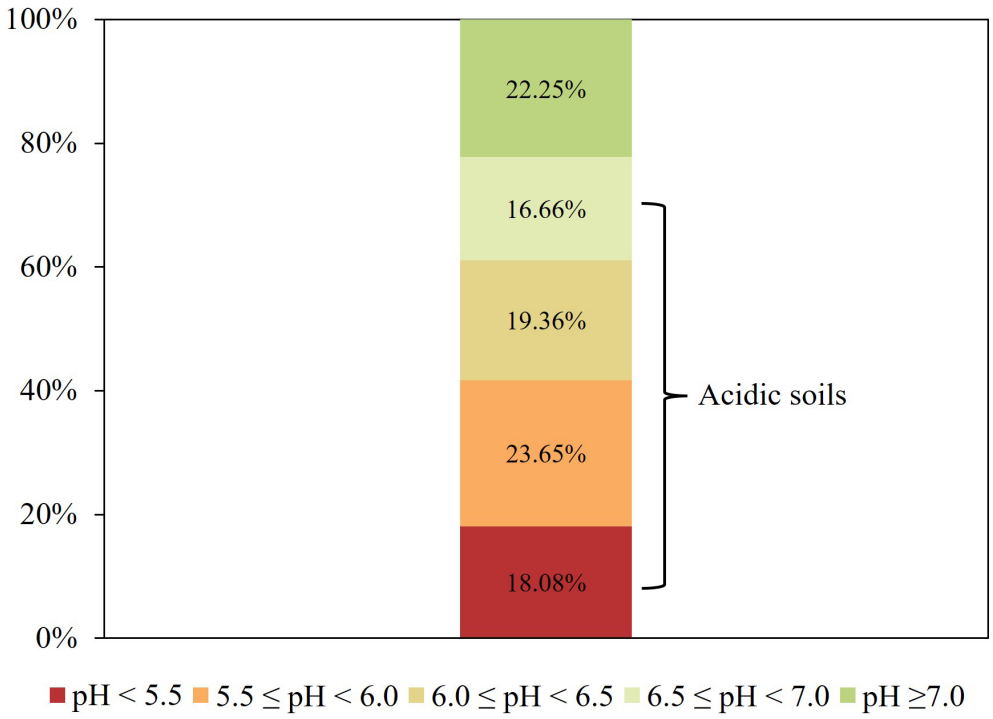
Supplementary Table 3 | CDR feedstock sensitivity settings.

Case	CaO (%)	MgO (%)	$R_{CO_2,max}$ (t CO_2 t^{-1} basalt)	Full weathering capacity at 50 t ha^{-1} (t CO_2 ha^{-1})	Relative to main CDR	Interpretation
Main basalt composition	5.30	2.40	0.1356	6.78	1.00×	Main gross CDR calculation
Chinese average basalt capacity sensitivity	9.10	7.35	0.3034	15.17	2.24×	CDR feedstock capacity sensitivity

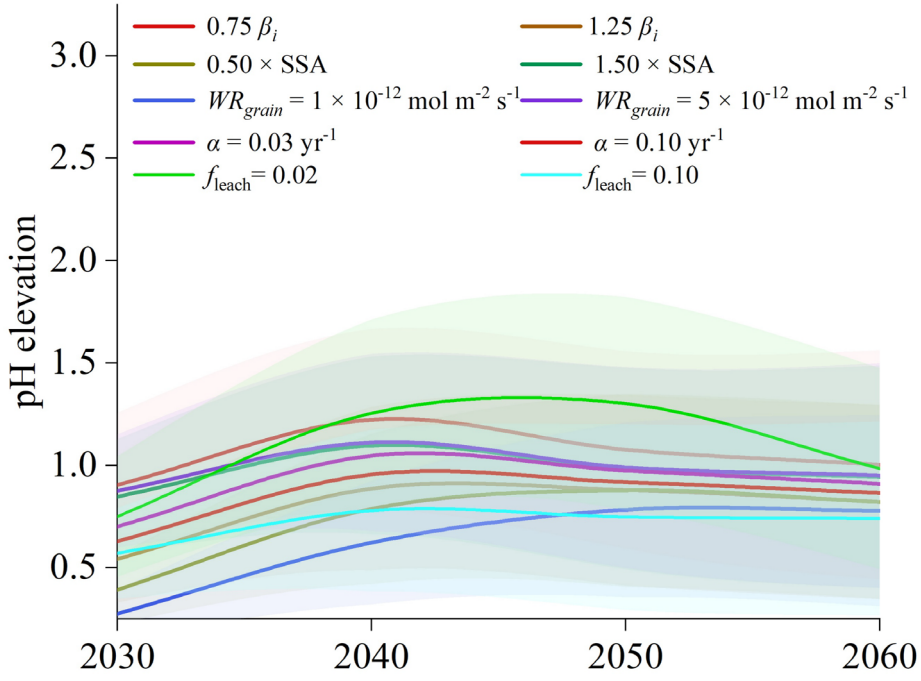
III. Supplementary Figures



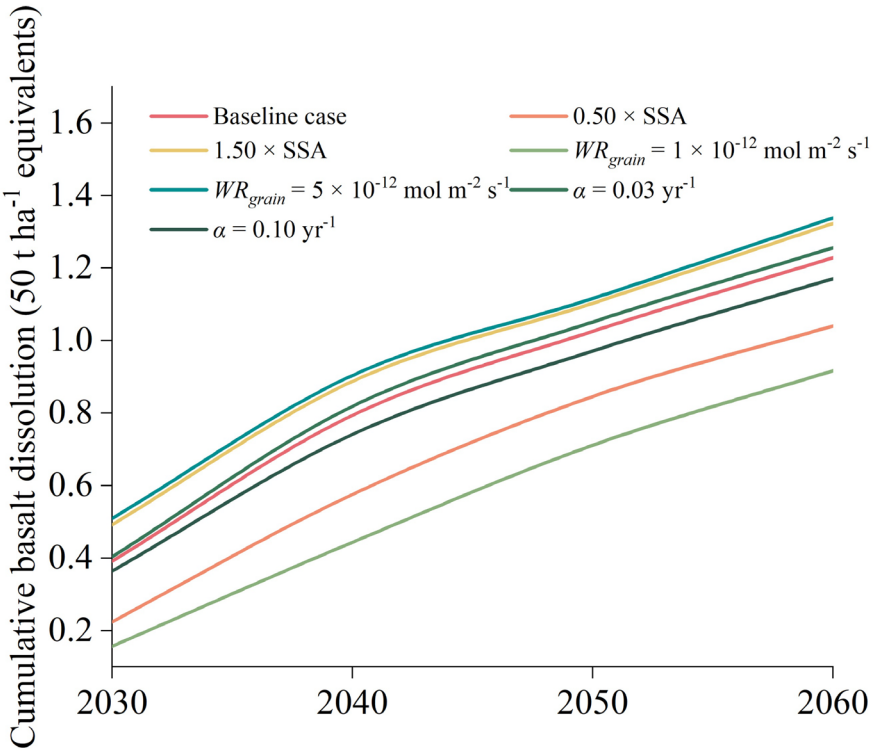
Supplementary Fig. 1 | Distribution of rice-growing regions and soil pH in China. Rice field distribution was acquired from Chinese Academy of Sciences Discipline Data Center for Ecosystem/National Ecosystem Science Data Center (https://www.nesdc.org.cn and https://doi.org/10.1088/1748-9326/ab80f0). National soil pH data was obtained from National Tibetan Plateau/Third Pole Environment Data Center (https://data.tpdc.ac.cn and https://doi.org/10.5194/essd-17-517-2025).



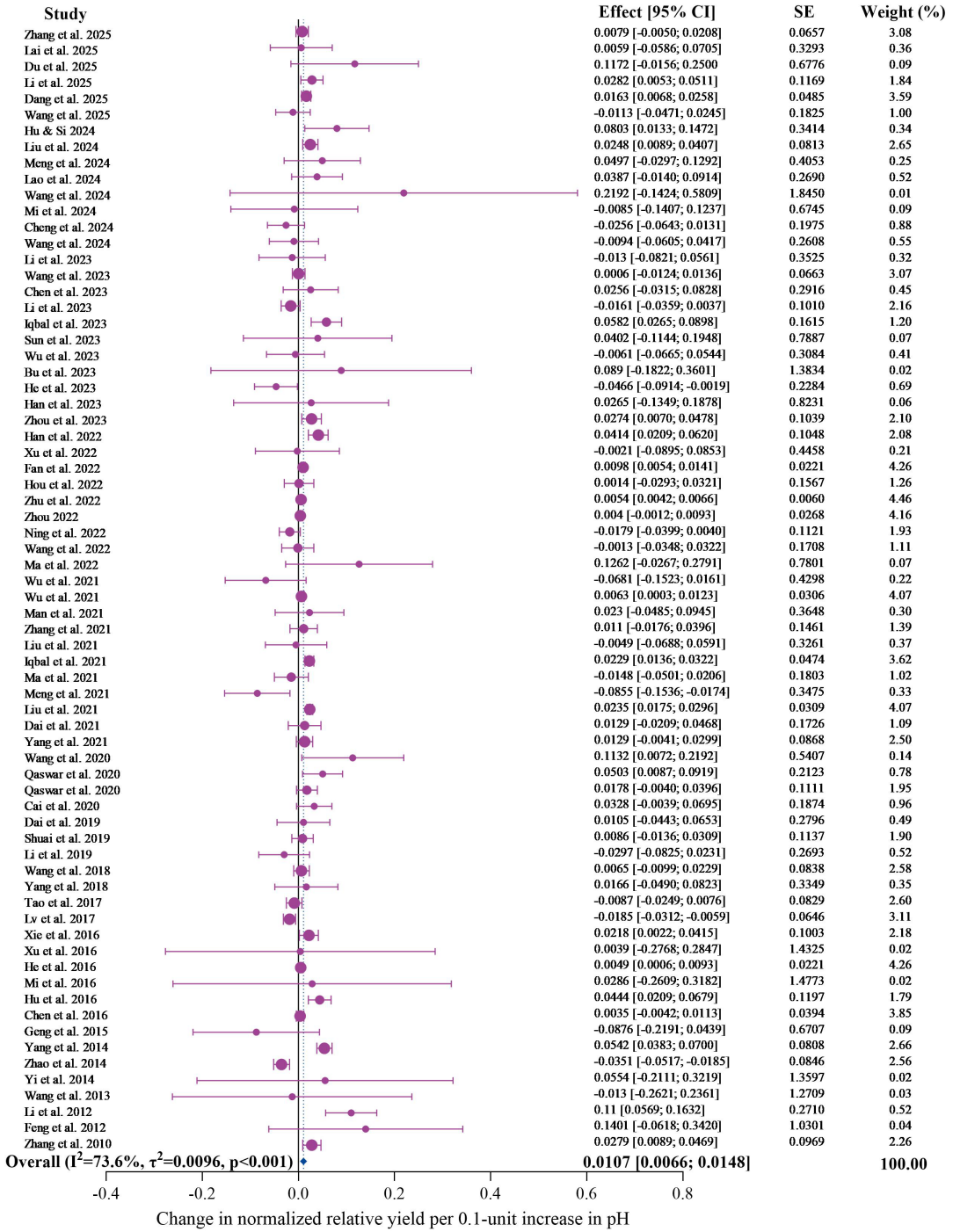
Supplementary Fig. 2 | Percentage of soil pH range in rice-growing areas of China.



Supplementary Fig. 3 | Sensitivity analysis of EW-driven soil pH elevation. Temporal trajectories of mean ΔpH from 2030 to 2060 under alternative assumptions for β_i, effective reactive surface area, WR_{grain}, α, and f_{leach}. Lines represent the mean ΔpH across acidic rice field grid cells, and shaded areas indicate the standard deviation (SD), reflecting spatial variability in modeled pH responses under each sensitivity case.

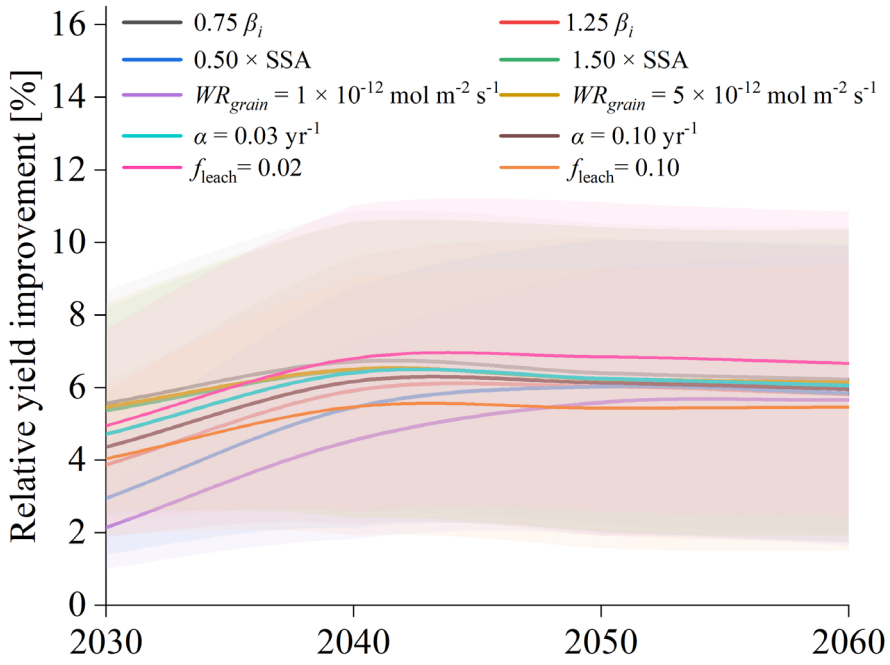


Supplementary Fig. 4 | Temporal evolution of mean cumulative basalt dissolution under different weathering assumptions. Curves represent the baseline case and sensitivity scenarios for specific surface area (SSA), WR_{grain}, and α. Values sum dissolved fractions across application cohorts, normalized to a single 50 t ha^{-1} application. Values exceeding 1.0 therefore reflect contributions from repeated applications.

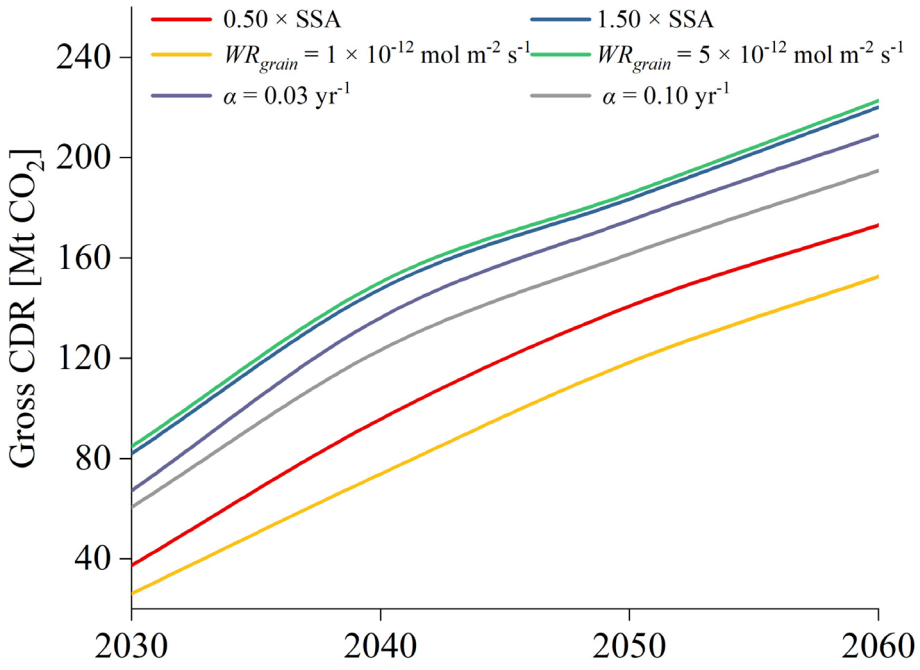


Supplementary Fig. 5 | Forest plot with random-effects meta-analysis. The left column, titled, "Study", lists the included papers. On the right, the "Effect" column shows the study-specific slopes [95% CI]. "SE" is standard error. The size of the circle indicates the weight, and the larger the circle, the greater the weight; percentage weight values are listed under the far-right column "Weight". The vertical line at X = 0 denotes the null line. The blue diamond at the bottom represents the pooled effect with a width of 95% CI, and the narrower the width, the higher the estimation precision. The position of the pooled effect is to the right of the null line, indicating a statistically significant positive correlation. The I^2 = 73.6% indicates that the magnitude of the soil pH effect on RY differed considerably among studies. This likely reflects real differences in soil conditions, management practices, cultivars, and experimental

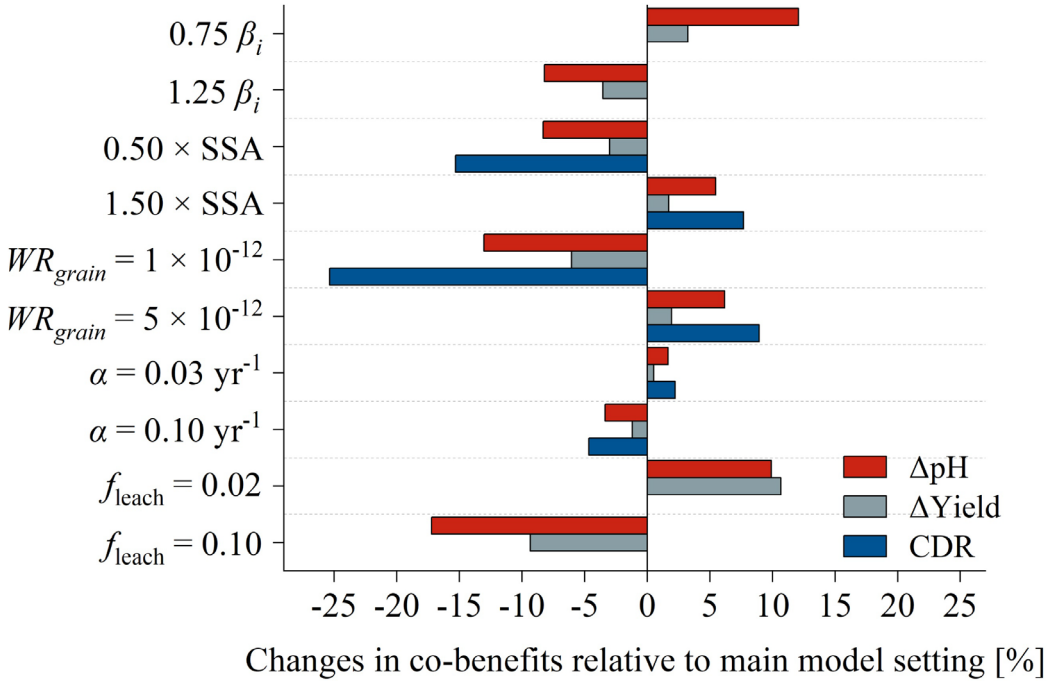
designs across the included studies, supporting the use of a random-effects model.



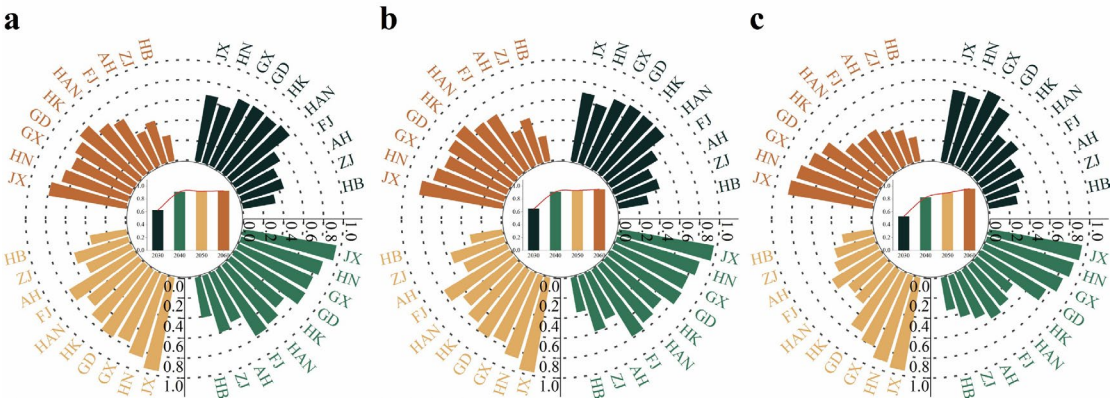
Supplementary Fig. 6 | Sensitivity analysis of EW-driven relative yield improvement. Changes in mean ΔRY from 2030 to 2060 under alternative settings for β_i, effective reactive surface area, WR_{grain}, α, and f_{leach}. Lines show the mean yield response estimated from pH changes, while shaded areas represent the SD for each case.



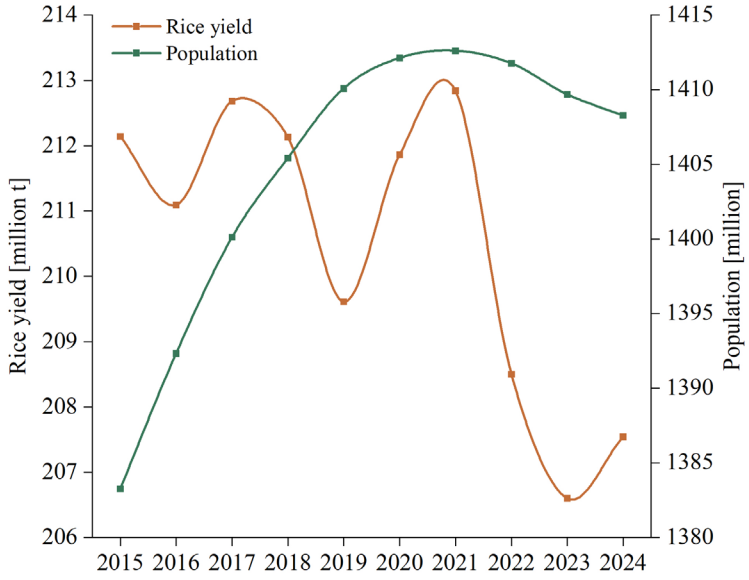
Supplementary Fig. 7 | Sensitivity of gross CDR to assumptions of weathering parameter. Temporal changes in gross cumulative CDR from 2030 to 2060 under alternative settings for effective reactive surface area, WR_{grain}, and α. Lines show national gross CDR totals across acidic rice fields for each sensitivity case.



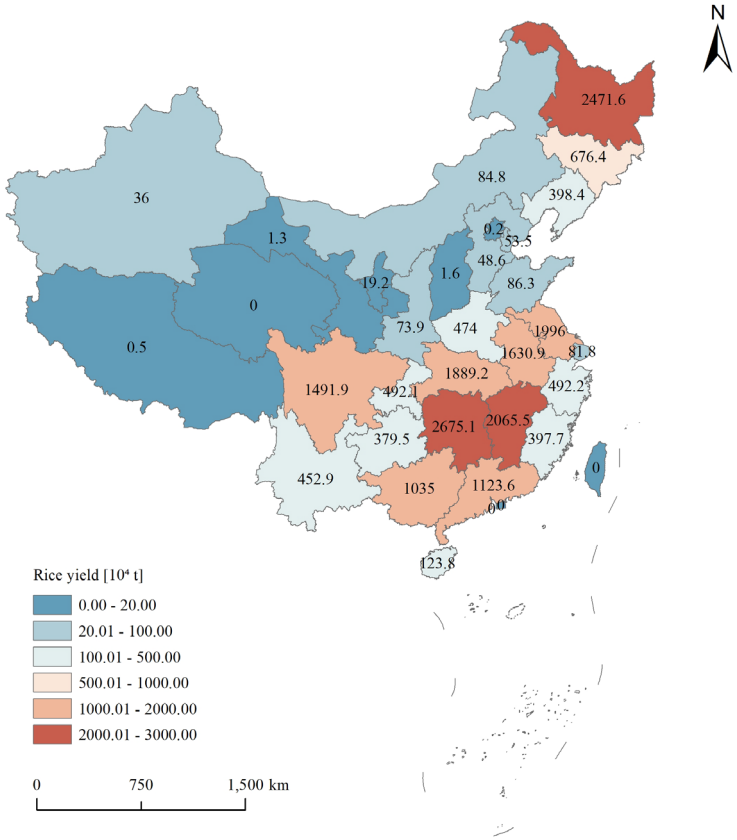
Supplementary Fig. 8 | Relative sensitivity of EW co-benefits to parameter assumptions in 2060. Percentage changes in ΔpH, ΔRY, and gross CDR relative to the baseline case setting under alternative assumptions for β_i, effective reactive surface area, WR_{grain}, α, and f_{leach}. Positive values indicate increases relative to the baseline case, whereas negative values indicate decreases. β_i affects ΔpH and ΔRY, but not gross CDR, because CDR is controlled by basalt dissolution and CaO/MgO derived feedstock capacity rather than the conversion of alkalinity to pH. For a fixed basalt application schedule, f_{leach} controls alkalinity retention and export without changing basalt dissolution or its associated gross CDR.



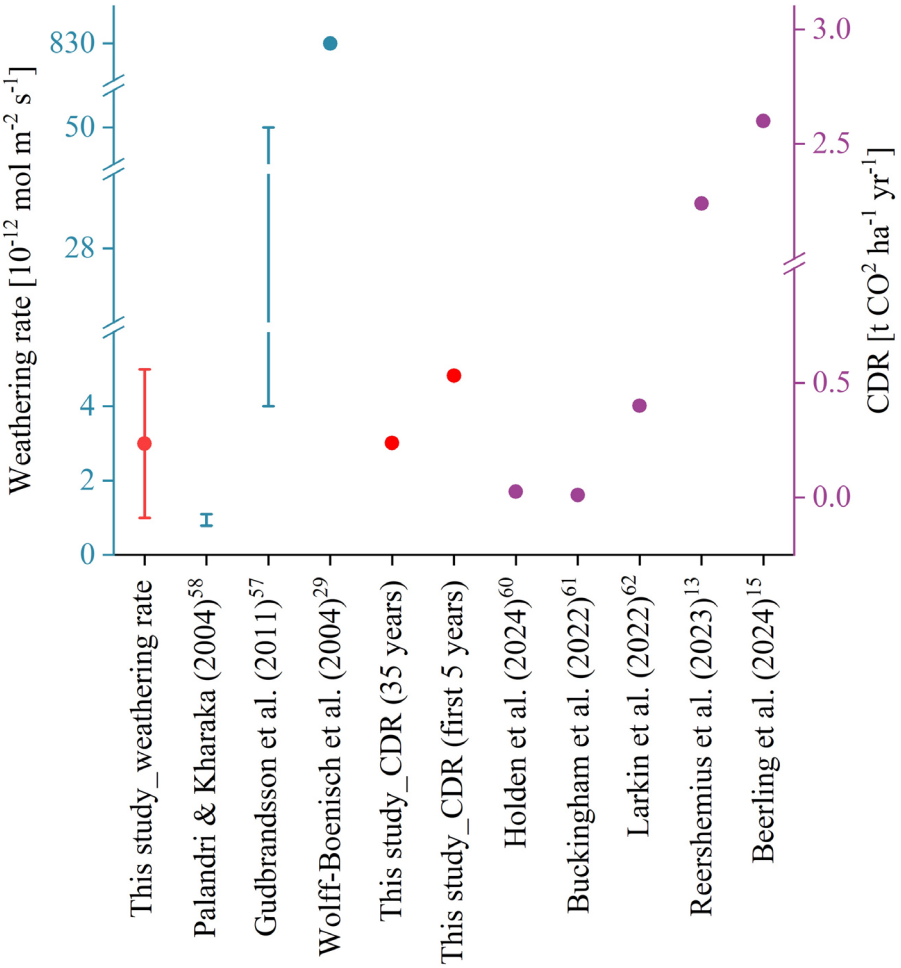
Supplementary Fig. 9 | Sensitivity of provincial CIC rankings to alternative weighting schemes. a-c pH priority weighting, yield priority weighting, and CDR priority weighting, respectively. Bars show normalized provincial CIC values and insets show the corresponding temporal change in overall CIC from 2030 to 2060 under each weighting scheme. The axis scale of CIC ranges from 0 to 1. The colors of the years in the central charts correspond to those in the surrounding provincial bar charts. The analysis tests whether regional prioritization is robust when greater emphasis is assigned to ΔpH, ΔRY, or gross CDR. Province abbreviations: JX, Jiangxi; HN, Hunan; GX, Guangxi; GD, Guangdong; HK, Hong Kong; HAN, Hainan; FJ, Fujian; AH, Anhui; ZJ, Zhejiang; HB, Hubei.



Supplementary Fig. 10 | Curve of China's population and actual rice yield from 2015-2024. The left y-axis represents actual rice yield. The right y-axis reflects changes in population. The x-axis indicates the latest available data for the past decade. Rice yield and population data in China were both derived from China Statistical Yearbook, National Bureau of Statistics of China (https://www.stats.gov.cn).



Supplementary Fig. 11 | Provincial rice yield statistics. Data sourced from China Statistical Yearbook, National Bureau of Statistics of China (https://www.stats.gov.cn).



Supplementary Fig. 12 | Literature comparison of weathering rate and CDR assumptions. The left side represents a comparison of the basalt grain-surface weathering rate used in this study with published laboratory dissolution rates for basaltic glass, crystalline basalt, and major basalt-forming silicate minerals. The red dot illustrates the reference value of "This study_weathering rate": WR_{grain} = 3 × 10^{-12} mol m^{-2} s^{-1}, with a sensitivity range of 1–5 × 10^{-12} mol m^{-2} s^{-1}. The right side represents a comparison of the area-normalized CDR rate from this study with published laboratory, field, and column-based EW estimates. The red dot's values from "This study_CDR (35 years)" are 0.2380 t CO_2 ha^{-1} yr^{-1} and "This study_CDR (first 5 years)" is 0.5308 t CO_2 ha^{-1} yr^{-1}, representing the average annualized gross CDR rate calculated from 204.39 Mt CO_2 over a 35-year period and 65.13 Mt CO_2 over the first 5 years, respectively, for 245409 km^2 of acidic rice fields.

IV. Supplementary References

1. Renforth, P. & Henderson, G. Assessing ocean alkalinity for carbon sequestration. *Rev. Geophys.* **55**, 636–674 (2017).

2. Andrews, M.G. & Taylor, L.L. Combating climate change through enhanced weathering of agricultural soils. *Elements* **15**(4), 253–258 (2019).

3. Kantola, I.B., Masters, M.D., Beerling, D.J., Long, S.P. & DeLucia, E.H. Potential of global croplands and bioenergy crops for climate change mitigation through deployment for enhanced weathering. *Biol. Lett.* **13**, 20160714 (2017).

4. Cong, L.H. et al. Harnessing enhanced rock weathering for carbon neutrality: potential and challenges in China. *Earth-Sci. Rev.* **271**, 105309 (2025).

5. Kantzas, E.P. et al. Substantial carbon drawdown potential from enhanced rock weathering in the United Kingdom. *Nat. Geosci.* **15**, 382–389 (2022).

6. Hartmann, J. et al. Enhanced chemical weathering as a geoengineering strategy to reduce atmospheric carbon dioxide, supply nutrients, and mitigate ocean acidification. *Rev. Geophys.* **51**, 113–149 (2013).

7. Beerling, D.J. et al. Potential for large-scale CO_2 removal via enhanced rock weathering with croplands. *Nature* **583**, 242–248 (2020).

8. Levy, C.R. et al. Enhanced rock weathering for carbon removal−monitoring and mitigating potential environmental impacts on agricultural land. *Environ. Sci. Technol.* **58**(39), 17215–17226 (2024).

9. Strefler, J., Amann, T., Bauer, N., Kriegler, E. & Hartmann, J. Potential and costs of carbon dioxide removal by enhanced weathering of rocks. *Environ. Res. Lett.* **13**, 034010 (2018).

10. Gaucher, Y., Tanaka, K., Johansson, D.J.A., Goll, D.S. & Ciais, P. Leveraging ecosystems responses to enhanced rock weathering in mitigation scenarios. *Nat. Commun.* **16**, 3021 (2025).

11. Rinder, T. & von Hagke, C. The influence of particle size on the potential of enhanced basalt weathering for carbon dioxide removal - Insights from a regional assessment. *J. Clean. Prod.* **315**, 128178 (2021).

12. Wang, Z.Y., Teng, F. & Reiner, D.M. Assessing the potential and cost of enhanced rock weathering in China. *Commun. Earth Environ.* (2026).

13. Reershemius, T. et al. Initial validation of a soil-based mass-balance approach for empirical monitoring of enhanced rock weathering rates. *Environ. Sci. Technol.* **57**, 19497–19507 (2023).

14. Kelland, M.E. et al. Increased yield and CO_2 sequestration potential with the C_4 cereal Sorghum bicolor cultivated in basaltic rock dust-amended agricultural soil. *Glob. Change Biol.* **26**, 3658–3676 (2020).

15. Beerling, D.J. et al. Enhanced weathering in the US Corn Belt delivers carbon removal with agronomic benefits. *Proc. Natl. Acad. Sci. U.S.A.* **121**(9), e2319436121 (2024).

16. Taylor, L. et al. Enhanced weathering strategies for stabilizing climate and averting ocean acidification. *Nat. Clim. Change* **6**, 402–406 (2016).

17. Beerling, D.J. et al. Transforming US agriculture for carbon removal with enhanced weathering. *Nature* **638**, 425–434 (2025).

18. Baek, S.H. et al. Impact of climate on the global capacity for enhanced rock weathering on croplands. *Earths Future* **11**, e2023EF003698 (2023).

19. Deng, H. et al. The environmental controls on efficiency of enhanced rock weathering in soils.

Sci Rep. **13**, 9765 (2023).
20. Xu, X., Wu, Z., Dong, Y., Zhou, Z. & Xiong, Z. Effects of nitrogen and biochar amendment on soil methane concentration profiles and diffusion in a rice-wheat annual rotation system. *Sci Rep.* **6**, 38688 (2016).
21. Lewis, A.L. et al. Effects of mineralogy, chemistry and physical properties of basalts on carbon capture potential and plant-nutrient element release via enhanced weathering. *Appl. Geochem.* **132**, 105023 (2021).
22. Beerling, D.J. et al. Challenges and opportunities in scaling enhanced weathering for carbon dioxide removal. *Nat. Rev. Earth Environ.* **6**, 672–686 (2025).
23. Murphy, B.W. Impact of soil organic matter on soil properties—a review with emphasis on Australian soils. *Soil. Res.* **53**, 605–635 (2015).
24. Helyar, K.R., Cregan, P.D. & Godyn, D.L. Soil acidity in New South Wales—current pH values and estimates of acidification rates. *Aust. J. Soil Res.* **28**, 523–537 (1990).
25. Pribyl, D.W. A critical review of the conventional SOC to SOM conversion factor. *Geoderma* **156**, 75–83 (2010).
26. Weaver, A.R. et al. Mapping soil pH buffering capacity of selected fields in the coastal plain. *Soil Sci. Soc. Am. J.* **68**, 662–668 (2004).
27. Maher, K. & Chamberlain, C.P. Hydrologic regulation of chemical weathering and the geologic carbon cycle. *Science* **343**,1502–1504 (2014).
28. White, A.F. & Brantley, S.L. The effect of time on the weathering of silicate minerals: why do weathering rates differ in the laboratory and field? *Chem. Geol.* **202**, 479–506 (2003).
29. Wolff-Boenisch, D., Gislason, S.R., Oelkers, E.H. & Putnis, C.V. The dissolution rates of natural glasses as a function of their composition at pH 4 and 10.6, and temperatures from 25 to 74°C. *Geochim. Cosmochim. Ac.* **68**(23), 4843–4858 (2004).
30. Gislason, S.R. & Oelkers, E.H. Mechanism, rates, and consequences of basaltic glass dissolution: II. An experimental study of the dissolution rates of basaltic glass as a function of pH and temperature. *Geochim. Cosmochim. Ac.* **67**(20), 3817–3832 (2003).
31. Maher, K., Rogers, B., Perzan, Z. & Kukla, T. Surface proton reservoirs constrain alkalinity export from enhanced weathering. *Environ. Sci. Technol.* **60**(34), 24044–24056 (2026).
32. te Pas, E.E.E.M., Chang, E., Marklein, A.R., Comans, R.N.J. & Hagens, M. Accounting for retarded weathering products in comparing methods for quantifying carbon dioxide removal in a short-term enhanced weathering study. *Front. Clim.* **6**,1524998 (2025).
33. Zheng, J.Q., Berns-Herrboldt, E.C., Gu, B.H., Wullschleger, S.D. & Graham, D.E. Quantifying pH buffering capacity in acidic, organic-rich Arctic soils: Measurable proxies and implications for soil carbon degradation. *Geoderma* **424**, 116003 (2022).
34. Wang, X., Tang, C., Mahony, S., Baldock, J.A. and Butterly, C.R. Factors affecting the measurement of soil pH buffer capacity: approaches to optimize the methods. *Eur. J. Soil Sci.* **66**, 53–64 (2015).
35. Curtin, D. & Trolove, S. Predicting pH buffering capacity of New Zealand soils from organic matter content and mineral characteristics. *Soil. Res.* **51**, 494–502 (2013).
36. DerSimonian, R. & Laird, N. Meta-analysis in clinical trials revisited. *Contemp. Clin. Trials* **45**, 139–145 (2015).
37. Borenstein, M., Hedges, L.V., Higgins, J.P.T. & Rothstein, H.R. A basic introduction to fixed-

effect and random-effects models for meta-analysis. *Res. Synth. Method.* **1**, 97–111 (2010).
38. Hartung, J. & Knapp, G. A refined method for the meta-analysis of controlled clinical trials with binary outcome‡. *Statist. Med.* **20**, 3875–3889 (2001).
39. IntHout, J., Ioannidis, J.P. & Borm, G.F. The Hartung-Knapp-Sidik-Jonkman method for random effects meta-analysis is straightforward and considerably outperforms the standard DerSimonian-Laird method. *BMC Med. Res. Methodol.* **14**, 25 (2014).
40. Holland, J.E. et al. Yield responses of arable crops to liming – An evaluation of relationships between yields and soil pH from a long-term liming experiment. *Eur. J. Agron.* **105**, 176–188 (2019).
41. Papke, L.E. & Wooldridge, J.M. Econometric methods for fractional response variables with an application to 401(k) plan participation rates. *J. Appl. Econ.* **11**, 619–632 (1996).
42. Renforth, P. The potential of enhanced weathering in the UK. *Int. J. Greenh. Gas. Con.* **10**, 229–243 (2012).
43. Renforth, P. The negative emission potential of alkaline materials. *Nat. Commun.* **10**, 1401 (2019).
44. Kroeger, J., Zhang, B.Q., Planavsky, N.J. & Yao, Y. Analyzing Co-Benefits and Rock Sourcing in Life Cycle and Techno-Economic Assessment of Enhanced Rock Weathering. *Environ. Sci. Technol.* **60**(8), 6215–6226 (2026).
45. Taylor, L.et al. Enhanced weathering strategies for stabilizing climate and averting ocean acidification. *Nat. Clim. Change* **6**, 402–406 (2016).
46. McBride, A.L. et al. Quantifying potential carbon dioxide removal via enhanced weathering using porewater from a field trial in Scotland. *Front. Clim.* **7**, 1606574 (2025).
47. He, L. L. et al. Meta-analysis of the effects of liming on soil pH and cadmium accumulation in crops. *Ecotox. Environ. Safe.* **223**, 112621 (2021).
48. Kong, L. et al. Factors influencing the effectiveness of liming on cadmium reduction in rice: A meta-analysis. *Sci. Total Environ.* **779**, 146477 (2021).
49. Yu, H. Y. et al. Arsenic mobility and bioavailability in paddy soil under iron compound amendments at different growth stages of rice. *Environ. Pollut.* **224**, 136–147 (2017).
50. Yamaguchi, N. et al. Arsenic release from flooded paddy soils is influenced by speciation, Eh, pH, and iron dissolution. *Chemosphere* **83**, 925–932 (2011).
51. Qiu, Y. et al. Intermediate soil acidification induces highest nitrous oxide emissions. *Nat. Commun.* **15**, 2802 (2024).
52. Khaliq, M. A. et al. Soil liming effects on CH_4, N_2O emission and Cd, Pb accumulation in upland and paddy rice. *Environ. Pollut.* **248**, 408–420 (2019).
53. Saisana, M., Saltelli, A. & Tarantola, S. Uncertainty and sensitivity analysis techniques as tools for the quality assessment of composite indicators. *J. R. Statist. Soc. A* **168**, 307–323 (2005).
54. Zhang, L. et al. Assessment of CO_2 mineral storage potential in the terrestrial basalts of China. *Fuel* **348**, 128602 (2023).
55. Paruolo, P., Saisana, M. & Saltelli, A. Ratings and rankings: Voodoo or science? *J. R. Statist. Soc. A* **176**, 609–634 (2013).
56. Greco, S., Ishizaka, A., Tasiou, M. & Torrisi, G. On the methodological framework of composite indices: A review of the issues of weighting, aggregation, and robustness. *Soc. Indic. Res.* **141**, 61–94 (2019).
57. Gudbrandsson, S., Wolff-Boenisch, D., Gislason, S.R. & Oelkers, E.H. An experimental study

of crystalline basalt dissolution from 2 ≤ pH ≤ 11 and temperatures from 5 to 75°C. *Geochim. Cosmochim. Ac.* **75**(19), 5496–5509 (2011).
58. Palandri, J.L. & Kharaka, Y.K. A compilation of rate parameters of water-mineral interaction kinetics for application to geochemical modeling. *U.S. Geological Survey, Menlo Park, CA* (2004).
59. Power, I.M. et al. Are enhanced rock weathering rates overestimated? A few geochemical and mineralogical pitfalls. *Front. Clim.* **6**, 1510747 (2025).
60. Holden, F.J. et al. In-field carbon dioxide removal via weathering of crushed basalt applied to acidic tropical agricultural soil. *Sci. Total Environ.* **955**, 176568 (2024).
61. Buckingham, F.L., Henderson, G.M., Holdship, P. & Renforth, P. Soil core study indicates limited CO_2 removal by enhanced weathering in dry croplands in the UK. *Appl. Geochem.* **147**, 105482 (2022).
62. Larkin, C.S. et al. Quantification of CO_2 removal in a large-scale enhanced weathering field trial on an oil palm plantation in Sabah, Malaysia. *Front. Clim*. **4**, 959229 (2022).